Developing and Benchmarking MH4D, a Tetrahedral Mesh MHD Code

Eric Meier

A thesis submitted in partial fulfillment of
the requirements for the degree of

Master of Science in Aeronautics and Astronautics

University of Washington

2008

Program Authorized to Offer Degree:

Department of Aeronautics and Astronautics

University of Washington
Graduate School

This is to certify that I have examined this copy of a master's thesis by

Eric Meier

and have found that it is complete and satisfactory in all respects, and that any and all revisions required by the final examining committee have been made.

Committee Members:

____

Uri Shumlak

____

Thomas Jarboe

Date: ______________________________________

In presenting this thesis in partial fulfillment of the requirements for a master's degree at the University of Washington, I agree that the Library shall make its copies freely available for inspection. I further agree that extensive copying of this thesis is only allowable for scholarly purposes, consistent with "fair use" as prescribed in the U.S. Copyright Law. Any other reproduction for any purposes or by any means shall not be allowed without my written permission.

Signature ______________________________

Date ________________________________

University of Washington

Abstract

Developing and Benchmarking MH4D, a Tetrahedral Mesh MHD Code

Eric Meier

Chair of the Supervisory Committee:
Professor Uri Shumlak
Aeronautics and Astronautics

The Plasma Science and Innovation Center (PSI-Center) is dedicated to developing predictive computational models for Emerging Concept plasma confinement experiments. The Center adopted MH4D, a finite volume tetrahedral mesh MHD code, largely for its facility in meshing and parallelizing geometrically complicated domains. New capabilities have been added to the code including periodic and electrically insulating boundary conditions, and atomic physics effects. Several benchmark calculations were done. The implicit and semi-implicit capabilities of the code were explored and developed. Preliminary simulations of the ZaP Flow Z-Pinch experiment were performed and compared to other reliable MHD simulation results. MH4D is limited in its ability to resolve fine detail, and time step limitations seem sure to prevent addition of important two-fluid physics. However, development has shown it to be a flexible test bed code – a useful tool for the PSI-Center's continuing mission.

TABLE OF CONTENTS

Page

LIST OF FIGURES

Figure Number Page

LIST OF TABLES

Table Number Page

ACKNOWLEDGMENTS

Of the Aeronautics and Astronautics faculty, the author would like to give special thanks to Professors Uri Shumlak, Tom Jarboe, Brian Nelson, and Research Scientist George Marklin for the patience and expertise that they have offered in support of this research. In addition, my thanks go to the PSI-Center Research Consultants for their devotion, to my fellow Research Assistants and Postdoctoral Research Associates, interaction with whom has been invaluable, to Roberto Lionello, Dalton Schnack, the initial developers of MH4D, to the DOE for supporting this work, and to my parents, family and friends who have always had confidence in me to pursue and reach my dreams.

Introduction

The first significant plasma science research was conducted in the 1920's by Irving Langmuir. Since then, many plasma applications have been commercialized – fluorescent lighting, plasma spray coating, and semi-conductor manufacturing to name a few. However, magnetic fusion energy (MFE), a plasma technology that would bring the power of stars to the earth, remains elusive. The United States has committed a large part of its MFE research budget to a single concept, the tokamak [1]. Because the commercial potential of the tokamak is uncertain, Emerging Concept (EC) devices, intended to be simpler and cheaper alternatives to the tokamak, are also being developed. The computational modeling research described in this thesis has been performed as part of the United States EC program.

Theorists have long relied on computation to improve comprehension of the intertwined electromagnetic and gas dynamic interactions in plasmas. Because of steadily increasing computer capability, it is now conceivable to simulate the overall behavior of plasma in an MFE device. Significant progress toward this goal has made, but integrated simulations that capture the small-scale and large-scale phenomena that determine confinement quality are still under development. The research for this thesis is part of the Plasma Science and Innovation (PSI) Center collaboration, which develops predictive computational models of emerging concept EC experiments [2].

The computational tool, MH4D (MagnetoHydrodynamics on a Tetrahedral Domain), is the basis for the research described in this thesis. MH4D solves the Resistive Magnetohydrodyamic (MHD) equations on a 3D tetrahedral mesh using a finite volume scheme. MH4D's irregular tetrahedral mesh facilitates grid generation for complicated asymmetric 3D geometries. When acquired by the

PSI-Center, the code was capable of simulations with resistivity and viscosity in domains with conducting boundaries. The following features have been added to the code:

- Periodic and electrically insulating boundary conditions
- Variable resistivity in the form of Spitzer and Chodura models
- Ohmic heating
- A simple atomic physics model, including ionization and recombination of a static neutral gas

Though the set of physics features in MH4D is smaller than for some similar established codes (e.g. NIMROD), if a user would like to capture first order Resistive MHD physics, the code's relative simplicity is attractive. Periodic and insulating boundary conditions can now be easily applied, and the capability of the code has been explored and expanded. MH4D is a useful code, especially as a test bed for new physics such as the atomic physics described in this thesis.

Several aspects of this research distinguish it from previous work:

1) This research involves full 3D MHD code development.

Full 3D codes (e.g. MACH3 [3] and WARP3 [4]) have previously been developed. However, fusion plasma simulation research has focused primarily on "spectral 3D" codes like NIMROD and M3D, which use 2D grids and resolve the 3rd dimension spectrally. (As discussed later in this section, MH4D is further distinguished from other full 3D code research by working with an irregular tetrahedral mesh.) As compared to full 3D codes, spectral 3D codes are more computationally efficient if low mode representation is adequate. Another advantage of the spectral approach is that only 2D grid generation is required. A limitation of spectral codes is that they require axisymmetry. Many MFE devices are non-axisymmetric. For example, consider the HIT-SI device, shown in Figure 1.

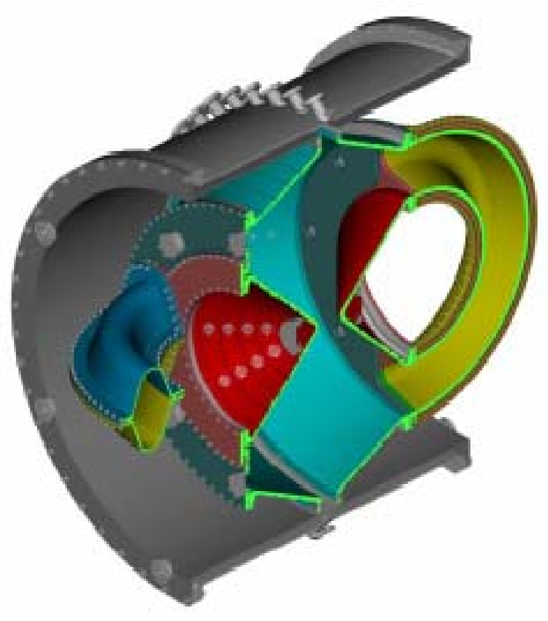

Figure 1: Cutaway view of the non-axisymmetric HIT-SI device. The non-axisymmetric injectors of HIT-SI can be modeled accurately with a "full 3D" code, but not with a "spectral 3D" code.

HIT-SI is not axisymmetric, but has been modeled with NIMROD [5]. In the NIMROD simulations, the non-axisymmetric injectors are not modeled accurately. The simulation results are interesting and useful in many ways, but disagreed with experimental evidence for toroidal current generation. Full 3D simulation results could provide better agreement with experimental data and greater insight into HIT-SI plasma behavior. This research contributes to the base of knowledge for full 3D MHD simulation.

2) Irregular tetrahedral meshes are used in this research.

MH4D uses a novel tetrahedral mesh MHD formulation. The primary impetus for the tetrahedral mesh formulation is that complicated 3D geometries can be easily discretized. Descriptions of tetrahedral mesh codes are not readily available in literature. References [10] and [11] discuss the numerical techniques employed in MH4D, but the implementation described uses a spectral 3D approach. This thesis presents unique research with tetrahedral mesh MHD simulations.

3) A simple atomic physics model that is tailored to EC devices has been implemented and tested in MH4D.

The effects of ionization, recombination and charge exchange can strongly influence plasma behavior in MFE devices. Most published atomic physics research focuses on the plasma edge regions of tokamaks and stellerators (see research involving the UEDGE code [6], for example). The research in this thesis describes an atomic physics implementation that is developed specifically for EC devices.

Chapter 1

MAGNETOHYDRODYNAMICS (MHD) IN GENERAL

Section 1.1 introduces the reader to magnetohydrodynamics (MHD), briefly describing its derivation from the particle picture. A more comprehensive derivation can be found Krall and Trivelpiece [7]. Section 1.2 presents validity limits for Resistive and Ideal MHD, largely following derivations by Freidberg [8]. Section 1.3 discusses these validity limits. In Section 1.4, the MHD validity limits are applied to three EC experiments, HIT-SI, ZaP, and TCS.

1.1 From N-body models to MHD

N-body models, which track individual particle motion, and kinetic models, which treat the plasma using probability distribution functions, are computationally demanding and generally can not be used to simulate magnetic fusion energy (MFE) devices. Fluid models are a common simplification of N-body models. The quantities that are commonly thought of as "fluid properties" – density, velocity, and temperature – are formally defined by taking moments of the probability distribution function of a plasma. Moments of the Boltzmann Equation, which is derived from a statistical plasma picture, produce the equations of the fluid models. The first three moments yield the density, momentum, and energy equations. Higher moments are possible, but these three are commonly used for a reasonably complete model that is computationally tractable. The equation set is closed with an equation of state – e.g. the adiabatic equation of state, $p \propto \rho^{\gamma}$. If the density, momentum and energy equations are tracked for ions and electrons, the equation set is called the Two-Fluid Model.

To reach the Full (Single-Fluid) Magnetohydrodynamic Model, or Full MHD, two “asymptotic approximations” are made:

1) Assume that the permittivity of free space is approximately zero. This enforces “quasineutrality” and eliminates displacement current in Ampere’s Law.
2) Assume that electron mass is approximately zero.

Implications of these approximations are discussed in Section 1.2. The first asymptotic approximation results in the low-frequency Maxwell’s equations,

$$\nabla \times \mathbf{B} = \mu_0 \mathbf{J},\ \nabla \times \mathbf{E} = -\frac{\partial \mathbf{B}}{\partial t},\ \nabla \bullet \mathbf{B} = 0\,. \tag{1}$$

In addition to these Maxwell’s equations, Full MHD has a density equation,

$$\frac{\partial \rho}{\partial t} = -\nabla \bullet \rho \mathbf{v}\,, \tag{2}$$

a momentum equation,

$$\rho\left(\frac{\partial \mathbf{v}}{\partial t} + \mathbf{v} \bullet \nabla \mathbf{v}\right) + \nabla p - \mathbf{J} \times \mathbf{B} = -\nabla \bullet \left(\vec{\vec{\boldsymbol{\pi}}}_i + \vec{\vec{\boldsymbol{\pi}}}_e\right) \tag{3}$$

an Ohm’s law (derivation of which involves neglecting electron momentum per the second asymptotic approximation),

$$\mathbf{E} + \mathbf{v} \times \mathbf{B} = \eta \mathbf{J} + \frac{1}{Zen}\left(\mathbf{J} \times \mathbf{B} - \nabla p_e - \nabla \bullet \vec{\vec{\boldsymbol{\pi}}}_e\right) \tag{4}$$

and a pressure equation,

$$\begin{aligned} \frac{d}{dt}\left(\frac{p}{\rho^\gamma}\right) = \frac{\gamma - 1}{\rho^\gamma}\Big[Q_{ei} + Q_{ie} - \nabla \bullet \left(\mathbf{h}_i + \mathbf{h}_e\right) - \vec{\vec{\boldsymbol{\pi}}}_i : \nabla \mathbf{v}_i - \vec{\vec{\boldsymbol{\pi}}}_e : \nabla \mathbf{v}_e\Big] \\ + \frac{\mathbf{J}}{Zen} \bullet \nabla\left(\frac{p_e}{\rho_e^{\ \gamma}}\right) \end{aligned}, \tag{5}$$

where $\overset{\leftrightarrow}{\boldsymbol{\pi}}_e$ and $\overset{\leftrightarrow}{\boldsymbol{\pi}}_i$ are anisotropic pressure tensors for the electrons and ions, η is electrical resistivity, Z is effective ion charge, e is electron charge, n is electron number density, $\mathbf{h}_e$ and $\mathbf{h}_i$ are heat fluxes for electrons and ions, and Q_{ei} and Q_{ie} represent electron-ion and ion-electron collisional heating. To reach the Ideal MHD model, all terms on right-hand sides of Eqns. (3), (4), and (5) are neglected. Of the terms neglected to reach the Ideal MHD, the Resistive MHD model retains the term involving electrical resistivity ($\eta\mathbf{j}$) in Eqn. (4) and an Ohmic heating term ($\sim \eta\mathbf{j}^2$) associated with Q_{ei}. Along with the modified Maxwell's equations as given in Eqn. (1), the Resistive MHD model uses Eqns. (2)-(5) in reduced form,

$$\begin{array}{ll}
\textit{Ohm's Law} & E = \eta\mathbf{J} - \mathbf{v}\times\mathbf{B} \\
\textit{Pressure} & \dfrac{\partial p}{\partial t} + \nabla \bullet (p\mathbf{v}) = (1-\gamma)\,p\nabla \bullet \mathbf{v} + (\gamma - 1)\eta\mathbf{j}^2 \\
\textit{Continuity} & \dfrac{\partial \rho}{\partial t} = -\nabla \bullet \rho\mathbf{v} \\
\textit{Momentum} & \rho\left(\dfrac{\partial \mathbf{v}}{\partial t} + \mathbf{v}\bullet\nabla\mathbf{v}\right) = -\nabla p + \mathbf{J}\times\mathbf{B}\,.
\end{array} \tag{6}$$

Resistive MHD provides the basis for MH4D. The particular form of the model used in MH4D is presented in Section 2.1.

1.2 Validity Limits of Ideal and Resistive MHD

Several assumptions were made in deriving Ideal MHD. Implications of these assumptions are discussed below, and key validity limits are presented. The basis for the limits is shown in some of the most important cases. Details supporting each validity limit can be found in reference [8].

To develop validity limits, it is necessary to define and specify several characteristic quantities for the plasma of interest. Characteristic time and length scales, τ and L, are set. Characteristic magnetic field, density, temperature, speed, and resistivity ($\mathbf{B}_0$, ρ_0, T_0, and V_0) are also defined. Although these scales and parameters are subjective choices[1], validity limits still provide valuable insight into MHD limitations.

Maxwellian distributions

In the process of deriving Ideal and Resistive MHD, Maxwellian distributions are assumed for ions and electrons. For these assumptions to be valid, electron and ion collisionality must be high: $\frac{\tau_{ii}}{\tau} \ll 1$ and $\frac{\tau_{ee}}{\tau} \ll 1$, where τ_{ii} is the ion-ion collision time, τ_{ee} is the electron-electron collision time, and τ is the characteristic timescale of phenomena of interest. The ion collisionality requirement,

$$\frac{\tau_{ii}}{\tau} \ll 1, \tag{7}$$

is more restrictive than the electron collisionality requirement.

First asymptotic approximation

Under the first approximation, Maxwell's equations are transformed to the low-frequency Maxwell's equations[2]. This is implemented by allowing the permittivity of free space to equal zero. Gauss's Law and Ampère's Law are modified. In

[1] For instance, the characteristic magnetic field, $\mathbf{B}_0$,, chosen for a Z-pinch might be the maximum field value. However, $\mathbf{B}$=0 at the center of a Z-pinch, so the choice for $\mathbf{B}_0$ is clearly not valid throughout the plasma. Similar general estimates are made for density, resistivity, and temperature for all experiments evaluated.

[2] As discussed, this approximation packages two simplifications: the assumption of quasineutrality and elimination of displacement current. These two simplifications can be considered independently as in reference [7].

Gauss's Law, which can be written $\varepsilon_0 \nabla \bullet \mathbf{E} = \sum_\alpha q_\alpha n_\alpha$, $\varepsilon_0 \approx 0$ means that $\sum_\alpha q_\alpha n_\alpha \approx 0$. This implements local quasineutrality, but does not require that $\nabla \bullet \mathbf{E} = 0$ or that $\mathbf{E}$ be restricted in any way. Next, consider Ampère's Law with the electric field split into dynamic and steady components, $\varepsilon_0 \left(\frac{\partial \mathbf{E}_s}{\partial t} + \frac{\partial \mathbf{E}_d}{\partial t} \right) = \frac{1}{\mu_0} \left(\nabla \times \mathbf{B} \right) - \mathbf{j}$. $\varepsilon_0 \approx 0$ does not pertain to $\mathbf{E}_\mathrm{s}$ because $\frac{\partial \mathbf{E}_s}{\partial t} = 0$ without the assumption. The dynamic electric field in Ampère's Law is eliminated, implying that electrons respond quickly to prevent local charge separation. Note that electric fields can still exist and evolve (slowly) under this first approximation.

The first approximation implies that $c^2 = \frac{1}{\mu_0 \varepsilon_0} \rightarrow \infty$ and $\omega_{pe}^2 = \frac{ne^2}{\varepsilon_0 m_e} \rightarrow \infty$. Therefore, only phenomena with characteristic speeds $V_0 \ll c$ and characteristic times $\tau \gg \frac{1}{\omega_{pe}}$ are captured under this assumption. It should be noted that high-frequency phenomena can affect low-frequency phenomena occurring on the timescale of interest. (High-frequency effects can sometimes be captured with transport coefficients such as resistivity as described in Section 3.4.)

Second asymptotic approximation

Under the second approximation, electron mass is set to zero. This approximation is natural since the ratio of proton mass to electron mass is 1836. However, electron mass causes finite response times which are significant, especially over long distances. Low-frequency, long-wavelength modes caused by electron lag, called drift waves, are missed in the MHD model because of this second approximation.

If $m_e \to 0$, clearly $\omega_{pe}^2 = \frac{ne^2}{\varepsilon_0 m_e} \to \infty$ and $\omega_{ce} = \frac{eB}{m_e} \to \infty$. It follows that electron skin depth, $l_e = \frac{c}{\omega_{pe}} \to 0$, electron Larmor radius, $r_{Le} = \frac{v_{th,e}}{\omega_{ce}} \to 0$, and Debye length, $\lambda_D = \frac{v_{th,e}}{\omega_{pe}} \to 0$. Therefore, only phenomena with $\tau \gg \left(\frac{1}{\omega_{pe}}, \frac{1}{\omega_{ce}} \right)$ and characteristic length $L \gg \left(l_e, r_{Le}, \lambda_D \right)$ are captured under this assumption. As mentioned above in the discussion of the first approximation, high-frequency phenomena can affect low-frequency phenomena.

Hall and diamagnetic terms

In Ohm's Law, $\mathbf{J} \times \mathbf{B} / Zen$ (the Hall term) and $\nabla p_e / Zen$ (the diamagnetic term) are neglected. Validity can be assessed by comparing these terms to a retained term in Ohm's Law, $\mathbf{v} \times \mathbf{B}$. These assumptions are valid if

$$\frac{\mathbf{J} \times \mathbf{B} / Zen}{\mathbf{vxB}} \sim \frac{\tau \omega_{ce} l_e^{\,2}}{L^2} \ll 1, \tag{8}$$

$$\frac{\nabla p_e / Zen}{\mathbf{vxB}} \sim \frac{r_{Li}}{L} \ll 1. \tag{9}$$

Infinite conductivity

In Ohm's Law, it is assumed that η=0. This assumption is valid if

$$\frac{\eta \mathbf{j}}{\mathbf{vxB}} \sim \frac{\eta}{\mu_0 L V_0} = \frac{1}{\mathrm{Re}_{mag.}} \ll 1. \tag{10}$$

Collisional heating

The collision heating terms, Q_{ei} and Q_{ie}, include the effects of Ohmic heating and from thermodynamic equilibration of the electron and ion species. If Eqn. (10) is violated, Ohmic heating should be included. Ions and electrons are in thermodynamic equilibrium if

$$\sqrt{m_i/m_e}\,\frac{\tau_{ii}}{\tau} \ll 1. \tag{11}$$

This thermodynamic equilibrium limit is more restrictive by $\sqrt{m_i/m_e}$ than the collisionality limit given by Eqn. (7).

Heat fluxes

$\nabla \bullet \mathbf{h}_e$ dominates the total heat flux $\nabla \bullet \left(\mathbf{h}_e + \mathbf{h}_i\right)$. The validity of neglecting $\nabla \bullet \mathbf{h}_e$ is assessed by comparing $\nabla \bullet \mathbf{h}_e$ to $\partial p/\partial t$. For validity, $\sqrt{m_i/m_e}\,\frac{\tau_{ii}}{\tau} \ll 1$. This limit is identical to the thermodynamic equilibrium limit, Eqn. (11).

Electron convection

The term $\frac{\mathbf{J}}{Zen} \bullet \nabla \left(\frac{p_e}{\rho_e^{\gamma}}\right)$ can be neglected if $\frac{r_{Li}}{L} \ll 1$. This is the same validity limit found for the diamagnetic term.

Anisotropic terms in energy equation

$\ddot{\boldsymbol{\pi}}_i : \nabla \mathbf{v}_i$ can be neglected if the ion collisionality limit, Eqn. (7), is satisfied. The requirement for neglecting $\ddot{\boldsymbol{\pi}}_e : \nabla \mathbf{v}_e$ is less restrictive.

1.3 Discussion of MHD validity limits

The high collisionality requirement is usually not met for fusion grade plasmas. However, empirical evidence indicates that Ideal/Resistive MHD are useful beyond the high collisionality validity limit. This circumstance arises because cyclotron motion plays the role of collisions in most fusion plasmas, and enhances the effective collisionality perpendicular to magnetic fields. In general, if parallel gradients are not expected, the collisionality assumption can be relaxed.

An important shortcoming of Ideal/Resistive MHD is an inability to capture local charge separation and the associated "two-fluid" effects such as the Lower Hybrid Drift instability.

To summarize, Ideal/Resistive MHD captures low-frequency, large-scale phenomena, and its simplicity makes it a valuable tool for understanding macroscopic plasma behavior.

1.4 Applicability of Ideal/Resistive MHD to EC devices

The validity limits found in Section 1.2 are now applied to several EC experiments: the HIT-SI spheromak, the ZaP Flow Z-Pinch and the TCS FRC. The characteristic parameters assumed for each device are summarized in Table 1.

Table 1: Characteristic parameters for HIT-SI, ZaP and TCS as used in MHD validity analysis. V_0 is the ion thermal speed. The characteristic time, τ, is L/V_0.

Scale or parameter	**HIT-SI**	**ZaP**	**TCS**
L (m)	0.1	0.01	0.1
B_0 (T)	0.03	1	0.02
n_0 (m^{-3})	$1x10^{19}$	$1x10^{23}$	$1x10^{20}$
T_0 (eV)	10	100	300
V_0 (m/s)	$4.4x10^4$	$1.4x10^5$	$2.4x10^5$

The ion-ion collision time, τ_{ii}, used in the analysis is found by using the relationship $\eta = \frac{\sqrt{m_i m_e}}{ne^2 \tau_{ii}}$. In this relationship, classical Spitzer parallel resistivity, $\eta = 5 \times 10^{-5} z \ln \Lambda / T^{3/2}$, is used.

As shown in Figure 2, the asymptotic approximations are reasonably valid for the devices considered. All validity limit values are less than 0.1. Most are less than 0.01.

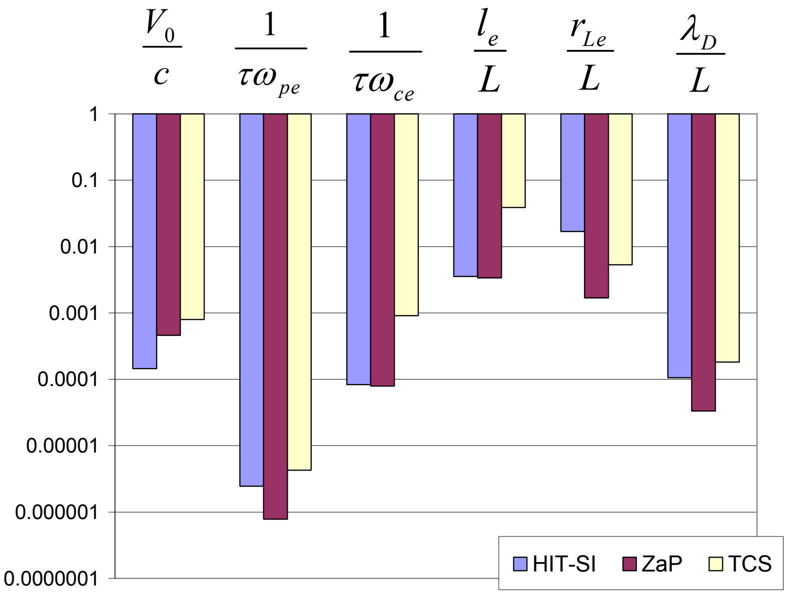

Figure 2: Asymptotic Approximation validity limits, evaluated for HIT-SI, ZaP and TCS. Values are much less than 1 in all cases, indicating that the Asymptotic Approximations are justified.

Validity limits for the simplification of Full MHD to Ideal MHD are evaluated and presented in Figure 3. The title "Collisionality" refers to the limit $\sqrt{m_i/m_e}\,\frac{\tau_{ii}}{\tau} \ll 1$. "Hall term" refers to $\frac{\tau\omega_{ce}l_e^2}{L^2} \ll 1$; "Diamagnetic term" refers to $\frac{r_{Li}}{L} \ll 1$; "Infinite conductivity" refers to $\frac{\eta}{\mu_0 L V_0} \ll 1$.

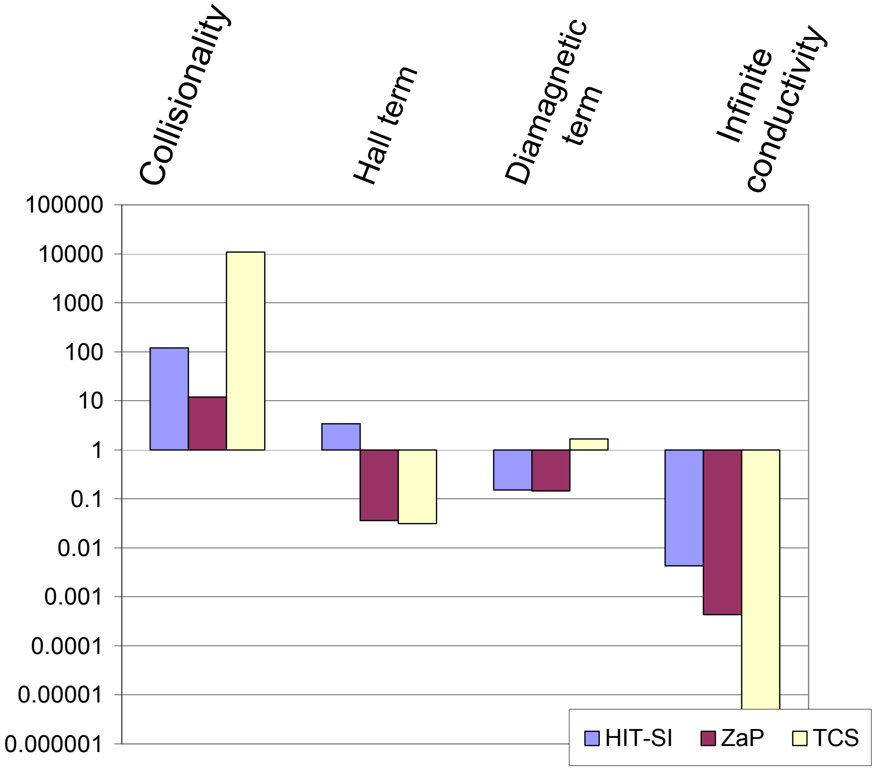

Figure 3: Validity limits for simplification of Full MHD to Ideal MHD for HIT-SI, ZaP and TCS. Collisionality and isotropy limits are not strictly satisfied for any of the devices. Neglecting the Hall term is clearly invalid for HIT-SI. Neglecting the diamagnetic term is clearly invalid for TCS.

Several aspects of the results presented in Figure 3 stand out:

- Clearly, the collisionality limit is violated for all three EC devices. However, as described in Section 1.3, collisionality is not required for ideal and resistive MHD to apply.

- The Hall term is clearly needed for HIT-SI and the diamagnetic term is clearly needed for TCS. MHD can provide insight into plasma dynamics in these devices, but potentially important effects could be missed.

- Figure 3 indicates that resistivity can be neglected in the three EC devices. Core plasma characteristics are assumed in Figure 3. However, plasma characteristics are dramatically different at the plasma edge and in near-vacuum regions, and the infinite conductivity validity limit is not applicable. For instance, in ZaP, high resistivity is appropriate in vacuum regions and in cool plasma.

Chapter 2

MH4D OVERVIEW

MH4D is a plasma simulation code that solves the resistive MHD equations with a finite volume method [23] on a tetrahedral mesh. The code is parallelized. T3D [24] is used to generate the mesh. ParMETIS [18] is used for partitioning. PETSc [26] is used for parallel matrix computations. Key algorithms include leapfrog time discretization, predictor-corrector advance to provide dissipation in the induction equation, and implicit treatment of dissipative terms. In this chapter, the features of MH4D that existed before adoption by the PSI-Center are presented, and some practical code application issues are discussed. Features that have been developed by the PSI-Center are described in Chapter 3.

2.1 MHD in original MH4D

MH4D originally used the following Resistive MHD model:

$$-\frac{\partial \mathbf{A}}{\partial t} = \mathbf{E}, \quad \mathbf{B} = \nabla \times \mathbf{A}, \quad \mathbf{j} = \nabla \times \mathbf{B} \tag{12}$$

Induction $$\frac{\partial \mathbf{A}}{\partial t} = \mathbf{v} \times \mathbf{B} - \eta \mathbf{j}$$

Pressure $$\frac{\partial p}{\partial t} + \mathbf{v} \bullet \nabla p = -\gamma p \nabla \bullet \mathbf{v}$$

Continuity $$\frac{\partial \rho}{\partial t} = -\nabla \bullet \rho \mathbf{v}$$

Momentum $$\rho\left(\frac{\partial \mathbf{v}}{\partial t} + \mathbf{v} \bullet \nabla \mathbf{v}\right) = -\nabla p + \mathbf{j} \times \mathbf{B} + \nu \nabla^2 \mathbf{v},$$

where **A** is the magnetic vector potential, **B** is the magnetic field, **E** is the electric field, **v** is velocity, **j** is current density, p is pressure, is ρ density, η is electrical resistivity, and ν is viscosity. **A** is the primitive variable for the electromagnetic components of the code. MH4D normalizes $\mathbf{j}$ and **B** by $\sqrt{\mu_0}$ so that μ_0 is left out of the computations. This results in conversions from "MH4D" units to S.I. units as shown in Appendix A.1.

MH4D uses a Cartesian coordinate system.

2.2 Tetrahedral mesh and finite volume formulation

MH4D uses an irregular tetrahedral mesh, a particularly useful mesh type when the computational domain involves complex geometric features. To generate a useful 3D mesh often requires separately discretizing different regions of the domain and then ensuring appropriate interfaces between the regions. With tetrahedra, the domain can be discretized as a single region and special interfacing is not required. Ease of grid generation comes at a price:

- Computational overhead is increased.
    - Reference arrays (see Appendix A.2) are required to describe the irregular grid. Logically mapped grids require no such arrays.
- Solution accuracy at a given resolution can be compromised.
    - Although first-order accuracy is maintained in a tetrahedral mesh with distorted tetrahedra, a uniform mesh may produce smoother solutions in general.

Eqns. (12) are solved in the order shown. Integral relations are used to define the operators. For example, the gradient is

$$\int_V (\nabla f)dV = \int_S (\mathbf{n}f)dS \tag{13}$$

In original MH4D algorithm development (i.e. before the research for this thesis began), special care was taken to preserve analytical properties of MHD in the discretized equations. In particular, the discretized spatial operators are self-adjoint [10]. Self-adjoint operators allow application of the efficient conjugate gradient method in iterative implicit solves.

Figure 4 shows a tetrahedron as used by MH4D. A staggered mesh or "dual mesh" is defined by the dashed lines between edge midpoints, side centroids and the cell centroid. Sides are labeled by the index of their opposite vertex. C is the centroid of the tetrahedron. m_{ij} is the midpoint of edge l_{ij}. C_i is the centroid of side *i.* S_i is the vector area of side *i.* s_i is the vector area of the dual mesh surface. Appendix A.3 provides additional geometric details which are used in the MH4D finite volume formulation.

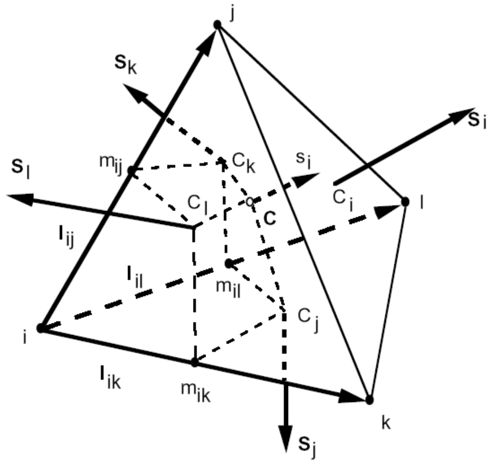

Figure 4: Staggered mesh used in MH4D. Vertices, edge lengths, tetrahedron surface areas, a dual mesh surface area, edge midpoints, face centroids, and the tetrahedron centroid are labeled.

As shown Figure 5, density, pressure and magnetic field are stored at cell centroids. Vector potential, momentum and current density are stored at vertices. Averaging is used to determine velocity at edge midpoints and at face centers as required for advection as described below.

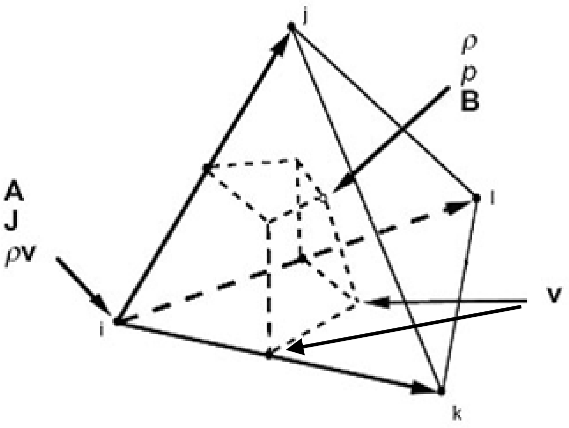

Figure 5: Variable storage locations. All variables are stored at either centroids or vertices. Velocity is averaged to centroids and faces for advection calculations.

Applying the finite volume method with **B** stored at tetrahedron centroids and **A** stored at vertices results in $\nabla \bullet \mathbf{B} = 0$ inside the domain. (No such guarantee exists for $\nabla \bullet \mathbf{B}$ on boundaries.) See Appendix A.3 for details.

The upwind method is used for advection. For example, the cell-to-cell advection formula for calculating $\nabla\bullet\left(\rho^{n-1/2}\mathbf{v}^{n}\right)$ for tetrahedron τ is

$$\frac{1}{V_\tau}\sum_{f}\left(\mathbf{v}_f\bullet\mathbf{S}_f\right)\rho_{upwind}\,, \tag{14}$$

where the sum is over the four tetrahedron faces, V_τ is the tetrahedron volume, $\mathbf{v}_f$ is the velocity averaged to the face, and $\mathbf{S}_f$ is the surface area vector of the face. The vertex-to-vertex formula for calculating $\mathbf{v}\bullet\nabla\mathbf{v}$ for vertex *v* is

$$\frac{1}{V_v}\sum_{e}\left(\mathbf{v}_e\bullet\mathbf{S}_e\right)\mathbf{v}_{upwind}\,, \tag{15}$$

where the sum is over the edges converging on the vertex, $\mathbf{v}_e$ is the velocity averaged to the edge midpoint, and $\mathbf{S}_e$ is the surface area vector of the edge as shown in Figure 6. The advected fields in Eqns. (14) and (15) are density and velocity, respectively, and the "upwind" subscripts indicate that the advected field values are taken from the "upwind" side of the control surface, i.e. the side for which $\mathbf{v}\bullet\mathbf{S}$ is positive.

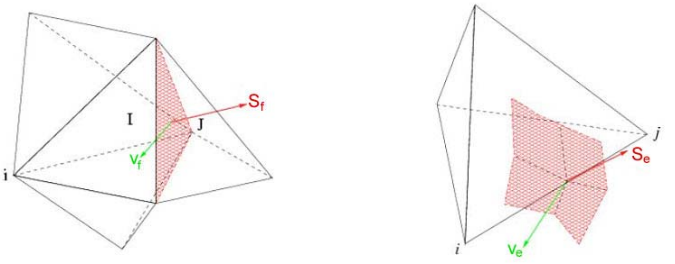

cell-to-cell advection
e.g. $\nabla\bullet\left(\rho^{n-1/2}\mathbf{v}^{n}\right)$

vertex-to-vertex advection
e.g. $\mathbf{v}\bullet\nabla\mathbf{v}$

Figure 6: Control surfaces for advection. Triangular areas between cells are used for cell-to-cell advection. Dual mesh areas converging on edges are used for vertex-to-vertex advection.

2.3 Time-stepping algorithm

The time-stepping algorithm for MH4D uses a leapfrog time discretization, defining **v** and **A** (along with p and ρ) on staggered intervals. Advective terms are advanced with a predictor-corrector method. Wave-like terms in the momentum equation can be treated with a semi-implicit method. Diffusive terms are treated implicitly. The algorithm is

$$\frac{\mathbf{A}^{*}-\mathbf{A}^{n-1/2}}{\Delta t}=\mathbf{v}^{n}\times\mathbf{B}^{n-1/2}, \tag{16}$$

$$\mathbf{B}^{*}=\nabla\times\mathbf{A}^{*}, \tag{17}$$

$$\begin{aligned}\frac{\mathbf{A}^{n+1/2}-\mathbf{A}^{n-1/2}}{\Delta t}&=\mathbf{v}^{n}\times\mathbf{B}^{*}\\&\quad-\eta\left[\theta_{i}\nabla\times\nabla\times\mathbf{A}^{n+1/2}-\left(1-\theta_{i}\right)\nabla\times\nabla\times\mathbf{A}^{n-1/2}\right],\end{aligned} \tag{18}$$

$$\frac{\rho^{n+1/2}-\rho^{n-1/2}}{\Delta t}=-\nabla\bullet\left(\rho^{n-1/2}\mathbf{v}^{n}\right), \tag{19}$$

$$\frac{p^{*}-p^{n-1/2}}{\Delta t}=-\nabla\bullet\left(p^{n-1/2}\mathbf{v}^{n}\right), \tag{20}$$

$$\frac{p^{n+1/2}-p^{*}}{\Delta t}=-\left(\gamma-1\right)p^{*}\nabla\bullet\mathbf{v}^{n}, \tag{21}$$

$$\frac{\mathbf{v}^{*}-\mathbf{v}^{n}}{\Delta t}=-\mathbf{v}^{n}\bullet\nabla\mathbf{v}^{n}, \tag{22}$$

$$\begin{aligned}\frac{\mathbf{v}^{**}-\mathbf{v}^{*}}{\Delta t}&=\frac{1}{\rho^{n+1/2}}\left(-\nabla p^{n+1/2}-\mathbf{j}^{n+1/2}\times\mathbf{B}^{n+1/2}\right)\\&\quad+\text{semi-implicit}\ ,\end{aligned} \tag{23}$$

$$\frac{\mathbf{v}^{n+1}-\mathbf{v}^{**}}{\Delta t}=\frac{\nu}{\rho^{n+1/2}}\left[\theta_{v}\nabla^{2}\mathbf{v}^{n+1}+(1-\theta_{v})\nabla^{2}\mathbf{v}^{**}\right]. \tag{24}$$

The theta method is used in the corrector step of the induction equation, Eqn. (18), and the viscous advance, Eqn. (24). θ_i and θ_v control the time weighting in the induction equation and viscous advances, respectively. The semi-implicit term shown in Eqn. (23) is discussed in Section 2.5. Implementation of the implicit procedure in the induction equation is discussed in Section 2.4. The time advance procedure is illustrated in Figure 7.

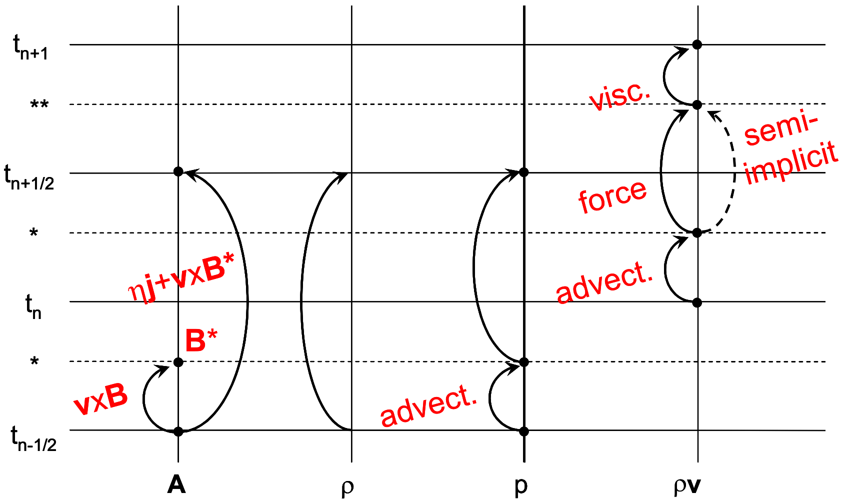

Figure 7: MH4D time step diagram. Vector potential is "predicted" with $\mathbf{v}^n \times \left(\nabla \times \mathbf{A}^{n-1/2}\right)$ and "corrected" with $\mathbf{v}^n \times \mathbf{B}^*$ and the implicit resistive term. Density is advanced in one flux step. Pressure is partially advanced with an advective step, and the advance is completed with $-\left(\gamma-1\right)p^*\nabla\bullet\mathbf{v}^n$. Velocity is advanced first with advection, then with force terms, then with the viscous term.

A more thorough discussion of the numerical techniques employed in time stepping can be found in reference [10].

2.4 Implicit resistive diffusion advance

An implicit advance of the resistive diffusion term of induction equation is appropriate when, because of numerical stiffness, excessive computational effort is required to advance the equation explicitly. Numerical stiffness in the induction equation is introduced by high resistivity. The $\eta\left(\nabla\times\nabla\times\mathbf{A}\right)$ term in the induction equation is diffusive as seen if a vector identity is used to rewrite the term as
$\eta\left(\nabla\times\nabla\times\mathbf{A}\right)=\eta\nabla\left(\nabla\bullet\mathbf{A}\right)-\eta\nabla^2\mathbf{A}$. The ∇^2 operator is the 3D equivalent of the spatial second derivative in the 1D diffusion equation, $\frac{\partial u}{\partial t}=D\frac{\partial^2 u}{\partial x^2}$, where u is a generic variable quantity and D is a diffusion coefficient. As shown in [25], the timestep limit

$$\Delta t\le\frac{\Delta x^2}{2D} \tag{25}$$

must be observed if the 1D diffusion equation is solved explicitly. In three dimensions, the Δx is replaced with the grid spacing, i.e. the distance between the vertices on which **A** is stored. For fine meshes, this diffusive timestep limit is often much more prohibitive than other timestep limits such as the Courant limits discussed in Section 2.5.

MH4D uses a θ-method for advancing **A**. In time-discretized form, the equation is

$$\frac{\mathbf{A}^{n+1/2}-\mathbf{A}^{n-1/2}}{\Delta t}=\mathbf{v}^n\times\mathbf{B}^*-\eta\left[\theta\nabla\times\nabla\times\mathbf{A}^{n+1/2}+\left(1-\theta\right)\nabla\times\nabla\times\mathbf{A}^{n-1/2}\right], \tag{26}$$

where $\mathbf{B}^*$ is $\nabla\times\mathbf{A}^*$ and $\mathbf{A}^*$ is computed with a predictor step,

$$\frac{\mathbf{A}^* - \mathbf{A}^{n-1/2}}{\Delta t} = \mathbf{v}^n \times \mathbf{B}^{n-1/2}.$$

A factor of dV (the dual mesh volume around each vertex) must be included on both sides of Eqn. (26) because of the finite volume integration technique used to form the $(\nabla\times\nabla\times)$ operator. The final form of the equation is

$$\underset{\mathbf{A}}{dV\left[\frac{\overleftrightarrow{\mathbf{I}}}{\eta} + \Delta t\theta\left(\nabla\times\nabla\times\right)\right]}\underset{\mathbf{x}}{\left(\mathbf{A}^{n+1/2} - \mathbf{A}^{n-1/2}\right)} \underset{=}{=} \underset{\mathbf{b}}{\frac{dV\Delta t}{\eta}\mathbf{v}^n \times \mathbf{B}^* - \Delta t dV \nabla\times\nabla\times\mathbf{A}^{n-1/2}} . \qquad (27)$$

A linear algebra problem, **Ax**=**b**, is formed. If θ is 0, the method is explicit. If θ is 1, the method is fully implicit and first-order accurate in time. Using θ = 1/2 corresponds to the Crank-Nicolson method which is second-order accurate in time. With θ ≥ 1/2, there is no stability criterion and timestep choice is guided by accuracy considerations.

Figure 8 depicts the matrix problem presented in Eqn. (27).

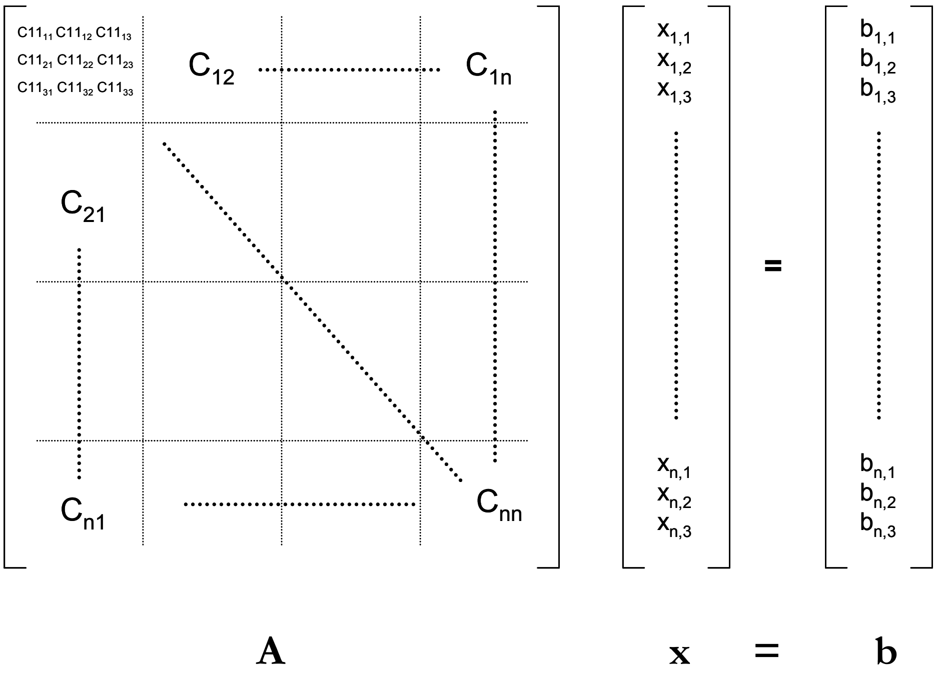

Figure 8: Basic matrix problem structure in MH4D. The matrix, A, is an n x n matrix of 3 x 3 coupling matrices, C_{ij}, coupling each vertex i to itself and all other vertices j. The components of vector quantities in x and b are labeled 1, 2 and 3.

For interior points, the vector components 1, 2 and 3 shown in Figure 8 are just the x, y, and z Cartesian components. For boundary points, vector quantities are stored in a rotated frame such that the z axis is normal to the boundary surface – in this rotated frame, vector components 1 and 2 are tangential to the boundary surface and component 3 is normal to the surface. This facilitates boundary condition application as discussed in Section 2.6.

The matrix **A** is symmetric positive definite: $C_{ii}=C_{ii}^T$ and $C_{ij}=C_{ji}^T$. Thus, convergence of the Conjugate Gradient method is guaranteed. MH4D uses PETSc to invert symmetric positive definite matrices using a preconditioned Conjugate Gradient method.

To understand the matrix shown in Figure 8, it is important to know the nature of the self-adjoint $dV\left(\nabla\times\nabla\times\right)$ operator. It is shown below operating on **A** to give $\mathbf{j}dV$ at vertex *i*:

$$\mathbf{j}_i dV_i = dV_i\left(\nabla\times\nabla\times\mathbf{A}_i\right) = -\frac{1}{9}\sum_\tau \frac{1}{V_\tau}\sum_v \left[\mathbf{S}_v^\tau\mathbf{S}_i^\tau - \left(\mathbf{S}_i^\tau \bullet \mathbf{S}_v^\tau\right)\mathbf{I}\right]\bullet \mathbf{A}_v^\tau \qquad (28)$$

where subscripts v and τ represent vertices and tetrahedra, **S** represents surface area vectors, and V is volume. The inner sum is over the vertices, *v*, of a tetrahedron, τ, and the outer sum is over the tetrahedra that share vertex *i*. The 3x3 coupling matrices C_{ij} shown in Figure 8 account for each contribution in Eqn. (28). Geometric details supporting Eqn. (28) and other MH4D finite volume relations are available in Appendix A.3.

2.5 Semi-implicit momentum advance

This section is an introduction to the semi-implicit advance used in MH4D. Details are provided in references [27], [28], and [29]. Validation of the semi-implicit method in MH4D for sound wave and Alfvén wave test problems is described in [30].

If the resistive term of the induction equation is treated implicitly and momentum is advanced explicitly, the algorithm shown in Section 2.3 is numerically stable if the simulation timestep satisfies the Courant conditions for waves and flows,

$$v_{\max}\Delta t < \Delta x \qquad (29)$$

where $v_{\max}$ depends on the flow speed, v_{flow}, and on the magnetosonic wave speed, $v_{MS} = \sqrt{{v_A}^2 + {v_S}^2}$, where the subscripts A and S refer to the Alfvén and sound speeds. $v_{\max}$ is defined by the geometric mean, $v_{\max} = \sqrt{v_{MS}^2 + v_{flow}^2}$. The magnetosonic wave speed is often much faster than the flow speed. However, using a semi-implicit method, the magnetosonic wave speed dependence in Eqn. (29) can be eliminated, leaving $v_{\max} = \left| v_{flow} \right|$.

The full MHD operator can separated into fast and slow components:

$$\frac{\partial u}{\partial t} = \underbrace{\mathcal{M}\{u\}}_{\text{full MHD operator}} = \underbrace{\mathcal{F}\{u\}}_{\text{Alfvén waves, soundwaves}} + \underbrace{\mathcal{S}\{u\}}_{\text{interesting physics}}. \tag{30}$$

Alfvén waves and sound waves are contained in $\mathcal{F}$, the fast part of the operator, while $\mathcal{S}$ contains the slower physics of interest. By treating $\mathcal{F}$ implicitly, the prohibitive wave Courant condition can be avoided. This procedure – treating fast waves implicitly and slow/interesting dynamics explicitly – is called semi-implicit[3]. Discretizing in time, treating the fast part implicitly (i.e. letting it operate on the velocity at time n+1), and treating the slow part explicitly,

$$\begin{aligned} \frac{u^{n+1} - u^n}{\Delta t} &= \mathcal{F}\left\{u^{n+1}\right\} + \mathcal{S}\left\{u^n\right\} = \mathcal{F}\left\{u^{n+1}\right\} + \left(\mathcal{M} - \mathcal{F}\right)\left\{u^n\right\} \\ &= \mathcal{M}\left\{u^n\right\} + \mathcal{F}\left\{u^{n+1} - u^n\right\} \end{aligned}, \tag{31}$$

This equation can be rewritten as a matrix problem for $u^{n+1} - u^n$,

[3] The semi-implicit method was developed for weather modeling, as described in [31], to eliminate the timestep restriction due to fast gravity waves.

$$\left(\mathbf{I}-\Delta t\mathcal{F}\right)\left(u^{n+1}-u^{n}\right)=\Delta t\mathcal{M}\left\{u^{n}\right\}. \tag{32}$$

$\mathcal{M}\left\{u^{n}\right\}$ is explicitly calculated, and the equation is solved implicitly for $u^{n+1}-u^{n}$ by inverting $\left(\mathbf{I}-\Delta t\mathcal{F}\right)$. $\mathcal{F}$ is chosen such that the matrix $\left(\mathbf{I}-\Delta t\mathcal{F}\right)$ is self-adjoint and can be solved with PETSc using a preconditioned Conjugate Gradient algorithm. Using the semi-implicit method, the computational effort can be significantly less than the effort required for an explicit advance.

The semi-implicit algorithm in MH4D was not used in this research. As mentioned above, the algorithm was used successfully in wave simulations, but additional research will be required to develop the algorithm for general applications like the benchmark simulations described in this research.

2.6 Boundary conditions

MH4D sets boundary conditions in two ways. *Explicit* boundary conditions are applied after explicit calculations, e.g. by zeroing normal components at boundaries. *Implicit* boundary couplings are modified in coupling matrices used in implicit advances that involve boundary points.

Nodes and sides are flagged in MH4D to facilitate boundary condition implementation. The code as originally adopted by the PSI-Center had only (perfectly) electrically conducting boundaries. All boundary nodes and sides are flagged. At all boundaries, vector quantities are stored in a rotated coordinate system with the z component normal to the surface[4].

[4] Domain corners present a challenge because the surface normal is undefined. Special treatment is often required at corners.

At perfectly conducting boundaries, tangential $\mathbf{E}$ must be zero. Thus, tangential components of $\frac{\partial \mathbf{A}}{\partial t}$ are set to zero[5].

The boundary condition for pressure is that the normal gradient is zero. Parallel velocity can be allowed on all boundaries (a slip boundary condition), or set to zero on all boundaries (a no-slip boundary condition). Normal velocity is set to zero on all conducting boundaries. Pressure and density flux are not allowed at any boundary.

Perfectly conducting wall boundary conditions are imposed in MH4D by default. For instance, before **v**x**B** is used to advance **A**, the subroutine zero_bndr_vv is called to zero the tangential components of **v**x**B** on boundaries. Also, zero_normal_vv is used to zero normal velocity at conducting boundaries. Non-default explicit boundary conditions are set using routines in setbc.f. For instance, special boundary conditions required at domain corners are imposed in setbc.f.

Conducting boundary conditions require $\mathbf{E}_{\text{tangential}} = 0$. Therefore, implicit boundary conditions are applied to the matrix $dV\left[\frac{\overleftrightarrow{\mathbf{I}}}{\eta} + \Delta t\theta\left(\nabla\times\nabla\times\right)\right]$ in Eqn. (27). Figure 9 illustrates the modifications made to impose conducting boundary conditions. Tangential components of conducting boundary vertices are decoupled from the equation system. Notice that the modified matrix remains symmetric positive definite.

[5] The condition $E_{\text{tangential}}$=0 corresponds to a fixed $A_{\text{tangential}}$ as shown in Eqn. 12.

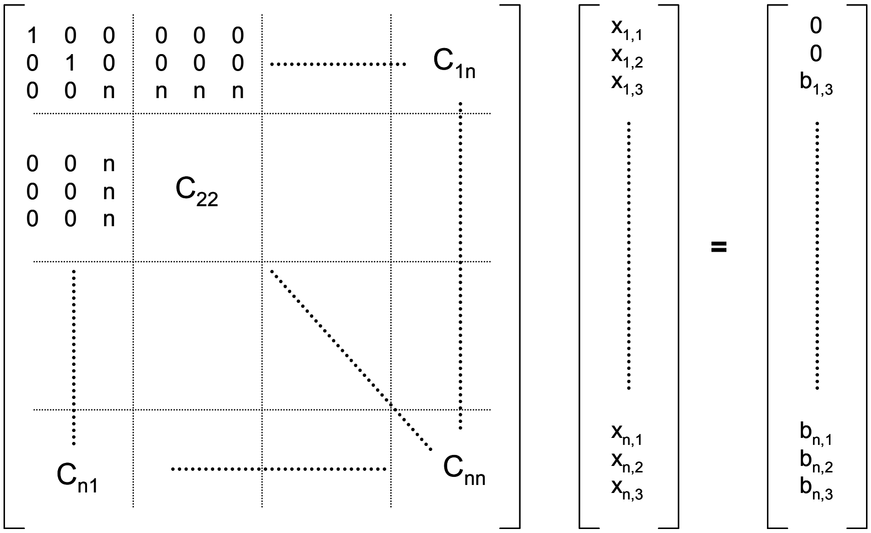

Figure 9: Operator matrix with conducting boundary condition imposed. Vertex 1 is on a conducting boundary. Vertex 2 is an interior vertex. Tangential components of conducting boundary vertices are decoupled.

2.7 Practical issues in MH4D simulations

Input deck

Through the input deck, all key variables can be set without recompiling the code.

Timestep

Typically, a small timestep (~10x less than the timestep required to satisfy stability limits) is used initially. The setdt routine allows the code to increase the timestep incrementally (the fractional increase never exceeding 10%) to the user-defined fraction of the timestep stability limit set with the input deck values, cflfac, cflfac_imp, or cflfac_si. The more restrictive of the wave/flow timestep limits and the resistive timestep limit is imposed by the setdt routine.

Grids and restart files

The grid generation program T3D [24] is used to create T3D files as described in Appendix B. A T3D file contains information about vertex/tetrahedron association and location. The "load" reads the T3D file and produces a "restart" file with grid information and MH4D primitive variable information in General Mesh Viewer (GMV) format [21] or in Tecplot [22] format. Data postprocessing involves reading restart files with GMV or Tecplot.

Different input parameters can be used with the load program to initialize a variety of problems. Reflect, shift, and rotate routines are available to manipulate the grid.

Memory considerations

MH4D is parallelized, and the memory requirements during the time stepping loop depend directly on the degree of parallelization. However, in the setup process, each processor temporarily creates and stores reference arrays and geometric factors describing the entire grid. Presently, setup is performed in parallel. For grids with many million tetrahedra, it may be important to modify MH4D so that setup processing occurs in serial so that memory limits are not exceeded.

Chapter 3

CODE DEVELOPMENT

3.1 Periodic boundary condition

Periodic boundary conditions are an important feature for a plasma simulation code. For example, computational expense can be reduced, mode selection is possible, and wave simulation is facilitated. The periodic boundary condition implemented in MH4D allows multi-direction periodicity which is needed for Alfvén wave simulation. The implementation also allows non-parallel-plane periodicity. Azimuthal sections of axisymmetric domains can be modeled, enabling mode selection and domain size reduction. For example if a 1/4-slice of a cylindrical domain is simulated, only *m*=0, 4, 8, etc. modes are captured.

In MH4D, periodicity has been implemented for pairs of periodic surfaces. One of the surfaces is designated “redundant” and the other, “retained”. On the retained surfaces, grid entities (vertices, triangular tetrahedral sides, and tetrahedral edges) are kept. On the redundant surfaces, redundant entity information is eliminated and replaced by pointers to the appropriate retained entities.

Two test problems were used to verify functionality of the parallel-plane periodic boundary condition: a sound wave and a shear Alfvén wave. For example, the Alfvén wave perturbation is

$$\mathbf{A}_1 = \frac{\varepsilon}{k}\cos(\mathbf{k}\bullet\mathbf{x}-\omega t)\,\hat{\perp}_1 \Rightarrow \mathbf{B}_1 = \varepsilon\sin(\mathbf{k}\bullet\mathbf{x}-\omega t)\,\hat{\perp}_2$$

$$\mathbf{v}_1 = \varepsilon\sin(\mathbf{k}\bullet\mathbf{x}-\omega t)\,\hat{\perp}_2 \qquad (33)$$

where $\hat{\perp}_2$ and $\hat{\perp}_1$ are in the transverse direction, ε is the perturbation size, $\mathbf{k}$ is a wavevector in the longitudinal direction. ($\left|\mathbf{k}\right| = \dfrac{2\pi n}{L}$ where n is the mode number and L is the periodic length.)

An obliquely propagating shear Alfvén wave in a triply periodic box domain was simulated successfully as depicted in Figure 10.

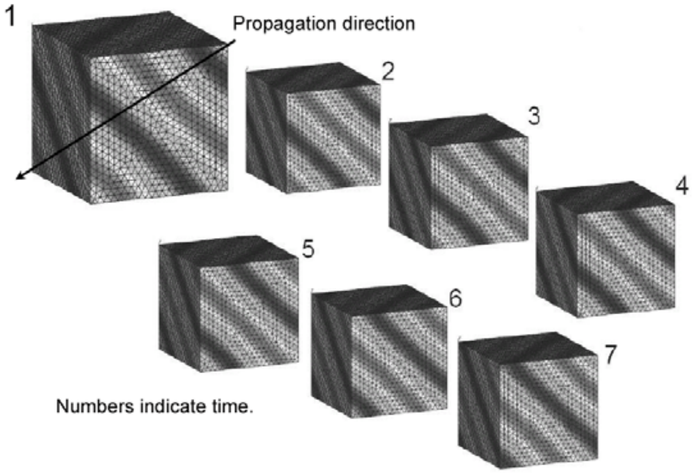

Figure 10: Perpendicular magnetic field strength contours for a shear Alfvén wave.

Non-parallel-plane periodicity is implemented by rotating vector quantities across the periodic boundary as appropriate, and by zeroing perpendicular components of vector quantities on the periodic axis. Rotations are simple in explicit calculations – the rotated (or inverse-rotated) quantity is multiplied by a rotation matrix. Rotations for matrix couplings across boundaries are more complicated. Consider the calculation

$$\mathbf{C}_{ij}\mathbf{x}_j = \mathbf{b}_i, \tag{34}$$

where $\mathbf{C}_{ij}$ is a 3x3 matrix which multiplies vector $\mathbf{x}_j$ to give vector $\mathbf{b}_i$. If the vector at vertex *j* is in a rotated frame defined by the rotation matrix $\mathbf{R}_j$, and the vector at vertex *i* is in a rotated frame defined by the rotation matrix $\mathbf{R}_i$, the calculation is

$$\mathbf{C}_{ij}\left(\mathbf{R}_j^T\mathbf{x}_j\right)=\left(\mathbf{R}_i^T\mathbf{b}_i\right), \tag{35}$$

where $\mathbf{R}^T$ is the transposed rotation matrix. This can be rewritten

$$\left(\mathbf{R}_i^T\mathbf{C}_{ij}\mathbf{R}_j^T\right)\mathbf{x}_j=\mathbf{b}_i\,. \tag{36}$$

The coupling matrix is pre-multiplied by $\mathbf{R}_i^T$ and post-multiplied by $\mathbf{R}_j^T$, and now vectors $\mathbf{x}_j$ and $\mathbf{b}_i$ are in their rotated frames. Additional care must be taken if the vectors **x** or **b** are on boundary points (recall that the boundary vectors are rotated such that their third vector component is normal to the surface). In this case, the inverse boundary rotation must take place before rotation across the periodic boundary.

3.2 Insulating boundary condition

An insulating-wall boundary condition has been added such that plasma interaction with electrically isolated electrodes can be modeled. To initially develop the boundary condition, a plasma-armature railgun was modeled as shown in Figure 11. The method was then extended to coaxial cylindrical shell electrodes and to ZaP simulations (see Chapter 6).

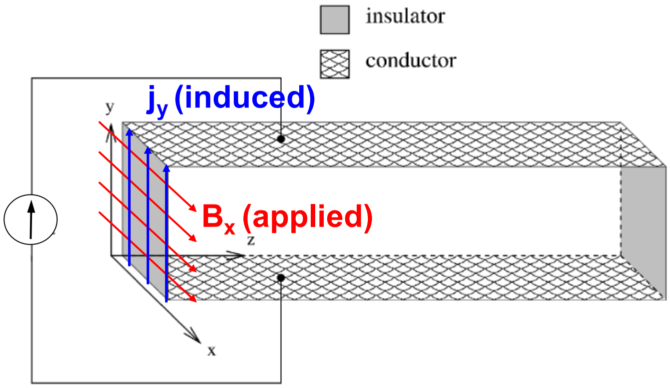

Figure 11: Plasma armature railgun problem with insulating boundary. Applied magnetic field, B_x, corresponds to a current source as shown. Top and bottom boundaries are electrically conducting. Gray-shaded boundaries are electrically insulating. The jxB force drags the applied B_x into the domain ("flux injection").

In general, either an electric or a magnetic field can be specified on the insulating boundary. If an electric field is specified, a fixed voltage across the electrodes is implied. If the magnetic field is specified, constant current is dictated between the electrodes. For instance, in coaxial geometry, $2\pi r B_\theta = \mu_0 I_{enclosed}$. In many plasma experiments, the power-supply has much higher impedance than the plasma, and the total current applied is a smoother function than the applied voltage. For this reason, the specified magnetic field boundary condition has been developed in MH4D.

Inside the domain, the current density at vertex *i* is calculated with the following formula:

$$\mathbf{J}_i = \frac{1}{3V_v}\sum_{\tau}\mathbf{S}_i \times \mathbf{B}_\tau\,, \tag{37}$$

where the sum is over tetrahedra that share vertex *i*, $\mathbf{S}_i$ is the surface area opposite vertex *i*, and V_v is the dual mesh volume around vertex *i*. Refer to Figure 4 for grid cell geometry. To implement the insulating boundary condition, the magnetic field on the insulating surface is included in the calculation:

$$\mathbf{J}_{i,i.b.} = \frac{1}{3V_v}\left(\sum_{\tau}\mathbf{S}_i \times \mathbf{B}_\tau + \sum_{i.b.}\mathbf{S}_{i.b.} \times \mathbf{B}_{i.b.}\right), \tag{38}$$

where the subscript i.b. means "insulating boundary", and the second sum is over all insulating boundary triangles that share vertex *i*.

At insulating boundaries, the velocity boundary condition is modified. A tangential electric field is induced by the applied magnetic field. In the induction equation ($\frac{\partial \mathbf{A}}{\partial t} = \mathbf{v}\times\mathbf{B} - \eta\mathbf{J}$), the tangential electric field is balanced by tangential components of **v**x**B** and η**J**. If normal velocity is zero, a tangential current must always exist on the insulating boundary. This non-physical current can be eliminated by allowing normal velocity on the insulating boundary[6]. Velocity away from the insulating walls reduces the density to zero at the wall. To prevent high Alfvén speeds and associated numerical stiffness in low-density plasma, a density floor is implemented as discussed in Section 3.3.

The implicit induction advance is modified to accommodate the insulating boundary. In the discretized induction equation, Eqn. (27), the $\nabla\times\nabla\times$ operators should include the tangential surface contributions. On the right-hand side,

[6] Velocity normal to a surface may seem non-physical. However, note that there is no *momentum* allowed through the wall. Even the density floor (see Section 3.3)only adds mass to the simulation.

$$\nabla\times\nabla\times\mathbf{A}=\left(\nabla\times\nabla\times\mathbf{A}\right)_{\text{internal}}+\left(\nabla\times\nabla\times\mathbf{A}\right)_{\text{boundary}}, \qquad (39)$$

where the insulating boundary term, $\left(\nabla\times\nabla\times\mathbf{A}\right)_{\text{boundary}}$ is $\frac{1}{3V_v}\sum_{i.b.}\mathbf{B}_{i.b.}\times\mathbf{S}_{i.b.}$ as found in Eqn. (38). On the left-hand side of Eqn. (27), $(\nabla\times\nabla\times)$ acts on $\left(\mathbf{A}^{n+1/2}-\mathbf{A}^{n-1/2}\right)$, so the surface part is $\frac{1}{3V_v}\sum_{i.b.}\left(\mathbf{B}_{i.b.}^{n+1/2}-\mathbf{B}_{i.b.}^{n-1/2}\right)\times\mathbf{S}_{i.b.}$. Assuming that $\mathbf{B}_{\text{i.b.}}$ is slowly varying on the boundary, Eqn. (27) is unchanged except for explicitly including the surface contribution for $\nabla\times\nabla\times\mathbf{A}^{n-1/2}$ per Eqn. (38). The implicit boundary conditions imposed on the $(\nabla\times\nabla\times)$ operator must be modified to allow for tangential components on the boundary. Recall that, as shown in Figure 9, tangential boundary components are decoupled for conducting boundary vertices. For insulating boundary vertices, tangential components remain coupled and normal components are decoupled as shown in Figure 12.

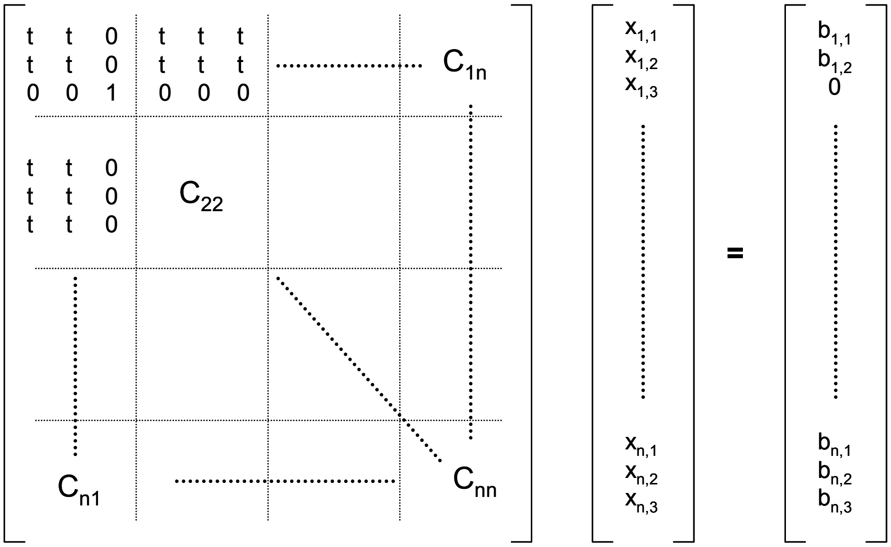

Figure 12: Operator matrix with insulating boundary condition imposed. Vertex 1 is on an insulating boundary. Vertex 2 is an interior vertex. Normal components of insulating boundary vertices are decoupled.

By decoupling normal components on the insulating boundary, a zero normal electric field boundary condition is imposed. This implies that surface charge is not allowed. Neglecting surface charge seems to be acceptable in the sense that flux is injected and the calculation is numerically stable. However, allowing surface charge (i.e. allowing normal components on the insulating boundary to couple) was not studied and could also give reasonable results.

If $\mathbf{B}_{i.b.}^{n+1/2}$ is known, the assumption of slow variation of $\mathbf{B}_{i.b.}$ is unnecessary. The contribution of the surface term, $\frac{1}{3V_v}\sum_{i.b.}\left(\mathbf{B}_{i.b.}^{n+1/2}-\mathbf{B}_{i.b.}^{n-1/2}\right)\times\mathbf{S}_{i.b.}$, is then added to the right-hand side.

3.3 Density floor

As density approaches zero, Alfvén speed $(v_A = |\mathbf{B}| / \sqrt{\mu_0 \rho})$ approaches infinity. After density is advanced, if density in any cell has dropped below some "density floor", mass is added at that cell to maintain the floor density. If the total mass contribution is small, this violation of continuity is acceptable.

3.4 Resistivity models and ohmic heating

Only uniform resistivity was available when the PSI-Center began developing MH4D. Options for Spitzer resistivity, Chodura resistivity, and a combination of the two have been added. Spitzer resistivity is defined by the well-known formula

$$\eta_{Sp.} = \frac{5\times10^{-5}\ln(\Lambda)}{T_{eV}^{3/2}}\,\Omega\text{-m} \tag{40}$$

The empirical Chodura resistivity model is designed to capture the anomalous resistivity that occurs at low densities. This anomalous resistivity is attributable to an instability when the electron drift speed exceeds the ion sound speed by a factor of ~3. This was shown by Shumlak et al. in simulations using a Two-Fluid plasma physics model [19] [20]. Chodura resistivity is implemented as

$$\eta_C = v_C \frac{m_e}{ne^2}\,;\; v_C = C_C \omega_{p,i}\left[1-\exp\left(-\frac{v_e}{f v_s}\right)\right] \tag{41}$$

where the electron drift speed and sound speed are $v_e = \frac{|\mathbf{j}|}{ne}$ and $v_s = \sqrt{\frac{\gamma p}{\rho}}$. The Chodura constant, C_c, and the parameter f, are typically $C_c \approx 0.1$ and $f \approx 3$.

Figure 13 compares Spitzer and Chodura resistivity graphically. As shown, Chodura exceeds Spitzer at high temperatures and low densities. To provide a smooth transition between high-temperature and low-temperature regimes, it is useful to combine the Chodura and Spitzer models. In MH4D the user can choose a combined model that sets resistivity to the higher of the Spitzer or the Chodura resistivity.

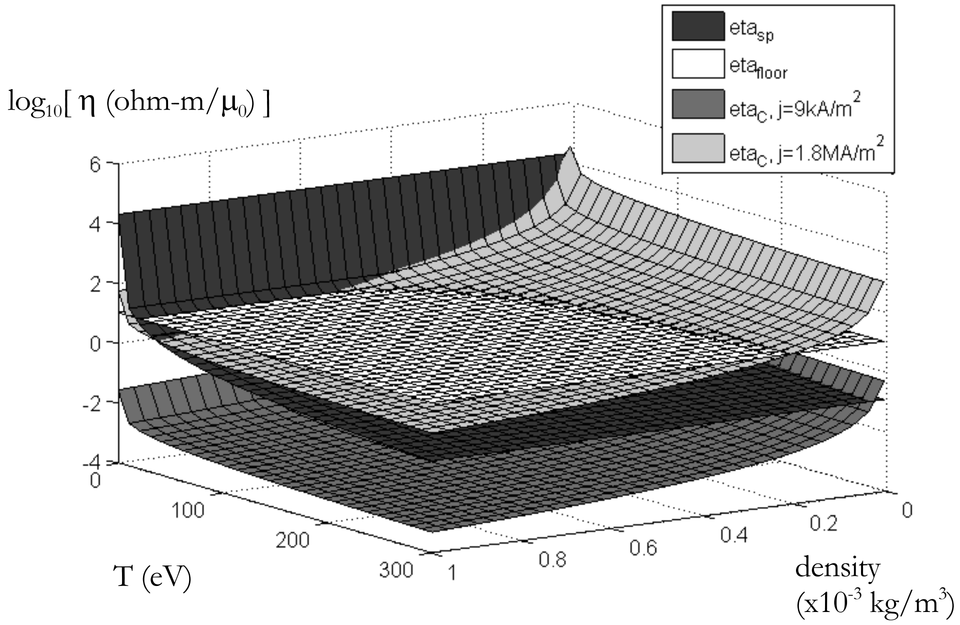

Figure 13: Comparison of Spitzer and Chodura resistivity models. Chodura resistivity is shown for two current density values. Chodura is greater than Spitzer at high temperatures and low densities.

When finite resistivity is present, it is appropriate to include the effect of collisional heating or "Ohmic" heating in the MH4D pressure equation shown in Section 2.1. Ohmic heating contributes energy $\eta \mathbf{j}^2$ to the system. The thermodynamic relation between energy and pressure is $e \sim \dfrac{p}{(\gamma - 1)}$, so the contribution of Ohmic heating to pressure is $(\gamma-1)\eta\mathbf{j}^2$. The modified pressure equation is

$$\frac{\partial p}{\partial t}+\mathbf{v}\bullet\nabla p=-\gamma p\nabla\bullet\mathbf{v}+(\gamma-1)\eta\mathbf{j}^2. \tag{42}$$

3.5 Atomic physics

Neutral gas atoms can have a significant effect on plasma behavior in magnetic confinement devices. Ionization cools the plasma. Ionized neutrals add mass with low momentum, slowing plasma motion. Recombination and charge exchange likewise play significant roles in plasma energy and momentum loss. By adding atomic physics effects in order of importance, the PSI-Center intends to develop an atomic physics model that allows predictive computational modeling of EC devices. An initial step has been to implement in MH4D a simple model involving a plasma fluid and a neutral fluid. The neutral fluid is assumed to be stationary and cold. The induction equation is unchanged for this atomic physics model. The new and modified equations are

$$\frac{\partial\rho_i}{\partial t}=-\nabla\bullet(\rho_i\mathbf{v}_i)\boxed{+\Gamma_{ion}-\Gamma_{rec}} \tag{43}$$

$$\boxed{\frac{\partial\rho_n}{\partial t}=-\Gamma_{ion}+\Gamma_{rec}} \tag{44}$$

$$\rho_i\frac{\partial\mathbf{v}_i}{\partial t}+\nabla(p_e+p_i)=\mathbf{j}\times\mathbf{B}\boxed{-\Gamma_{rec}m_i\mathbf{v}_i} \tag{45}$$

$$\frac{\partial p}{\partial t}+\mathbf{v}\bullet\nabla p=-\gamma p\nabla\bullet\mathbf{v}+(\gamma-1)\eta\mathbf{j}^2\boxed{-(\gamma-1)\Gamma_{ion}m_n\Phi_{ion}-\Gamma_{rec}m_i p}. \tag{46}$$

Eqns. (43)-(46) are ion continuity, neutral continuity, ion momentum, and ion pressure. Modifications to the usual MH4D MHD model are shown in boxes. Γ_{ion} and Γ_{rec} are the source rates for ionization and recombination in $kg/\left(m^3 s\right)$. For example, $\Gamma_i = \langle \sigma_{ion} \mathbf{v}_e \rangle \rho_i n_n$, where σ_{ion} is the ionization cross section and $\langle \sigma_{ion} \mathbf{v}_e \rangle$ is the ionization rate parameter. The angle brackets indicate that the quantity has been averaged over a Maxwellian distribution. Charge exchange is assumed to be zero in this implementation, but could easily be added. Ionization and recombination rates are temperature dependent per the following relations for coronal equilibrium given by Goldston and Rutherford [9]:

$$\langle \sigma_{ion} \mathbf{v}_e \rangle = \frac{2\times10^{-13}}{6.0 + T_{e,eV}/13.6} \left(\frac{T_{e,eV}}{13.6}\right)^{1/2} \exp\left(-\frac{13.6}{T_{e,eV}}\right) \text{ m}^3\text{s}^{-1} \tag{47}$$

$$\langle \sigma_{rec} \mathbf{v}_e \rangle = 0.7\times10^{-19} \left(\frac{13.6}{T_{e,eV}}\right)^{1/2} \text{ m}^3\text{s}^{-1} \tag{48}$$

Simple ion and neutral accounting rules are observed in MH4D. If $\Gamma_{ion} dt$ is greater than ρ_n, $\rho_i = \rho_i + \rho_n$ and $\rho_n = 0$. Likewise, if $\Gamma_{rec} dt$ is greater than ρ_i, $\rho_n = \rho_n + \rho_i$ and $\rho_n = \rho_{floor}$.

Timestep restrictions associated with atomic physics timescales are discussed in Section 5.1.

A limitation of this atomic physics model is that Paschen physics (i.e. the cascade of secondary electrons emitted by collisions in an interelectrode gap) is not captured. However, as shown in the applications of this model (see Chapter 5 and Section 6.6), important atomic physics effects are still captured.

Chapter 4

SCREW PINCH AND SPHEROMAK BENCHMARKS

4.1 Screw Pinch

As a code benchmark test, the linear phase of the *m*=1 screw pinch kink instability was simulated with MH4D. The instability growth rates found with MH4D are compared to growth rates found with a linear stability analyzer which uses the linearized MHD equations and captures only *m*=1 modes.

4.1.1 Theoretical Background

Equilibrium in a screw pinch is governed by the equation

$$\mathbf{j}\times\mathbf{B}=\nabla p \tag{49}$$

There are three variables: p, the plasma pressure, B_θ, the azimuthal magnetic field, and B_z, the axial magnetic field. (Radial magnetic field is zero.) If any two of these are specified, the third is determined by the equilibrium equation.

Beginning with an equilibrium, we expect an external current-driven kink instability in a screw pinch if the axial magnetic field is too weak [13] [14]. The requirement for kink stability is quantified as follows:

$$q=\frac{B_z/\left(L\right)}{B_\theta/(2\pi a)}>1 \tag{50}$$

If a kink perturbation is present, magnetic energy is converted to kinetic energy when q<1, but if q>1, magnetic energy is increased at the expense of perturbation energy. Detailed explanations of the screw pinch kink can be found in [15] and [16].

A parabolic pressure profile was chosen for the screw pinch benchmark: $p = p_0\left[1-\left(\frac{r}{a}\right)^2\right]$. Constant temperature is assumed, and density is determined by the ideal gas law. Given a parabolic pressure profile, Eqn. (49) can be solved to find the equilibrium magnetic field profile,

$$B_\theta = \begin{cases} \frac{r}{a}\sqrt{p_0\mu_0} & \mathrm{r} \le \mathrm{a} \\ \frac{a}{r}\sqrt{p_0\mu_0} & \mathrm{r} > \mathrm{a} \end{cases}. \tag{51}$$

4.1.2 MH4D modeling of the screw pinch

For this screw pinch problem, T3D was used to generate a discretized cylindrical domain. The load program was then used to load initial data, make the cylinder ends periodic, and generate a restart file in GMV format. The following parameters were chosen: cylinder length = 0.1 m; cylinder diameter = 0.1 m; pinch radius, a=0.03 m; p_0=1x10^6 Pa; T=50 eV (ρ_{max} = 1.05x10^{-4} or n_{max}=6.29x10^{22}).

To assign initial vector potential, $\mathbf{A_0}$, in the restart file, it is necessary to determine an $\mathbf{A_0}$ that satisfies $\mathbf{B}_0 = \nabla\times\mathbf{A}_0$. Knowing the form of the curl in cylindrical coordinates, a suitable $\mathbf{A_0}$ can be found. In this case, only B_θ exists, so $B_\theta = \frac{\partial}{\partial z}A_r - \frac{\partial}{\partial r}A_z$. Choosing A_r=0, one can solve for A_z, and use the value in the restart file. In the first timestep of the simulation, MH4D computes **B**.

A helical velocity perturbation was used, $v = 0.01 v_A$. The Alfvén speed used for the perturbation (and for the growth rate normalization, below) is based on the azimuthal magnetic field strength and density at r=a/2. Ideal MHD was used in these simulations. The cylinder ends were periodic. The default conducting boundary condition is applied at the cylinder outer wall.

4.1.3 Results and Discussion

Table 2 shows the normalized kinetic energy growth rates found with MH4D and the normalized kink instability growth rates found with a linear stability analyzer (developed by the author).

Table 2: MH4D screw pinch kinetic energy growth rates compared to kink instability growth rates predicted with linear stability code "linstab". Agreement is within 5%.

q	Linstab $\gamma\tau_A$	MH4D $\gamma\tau_A$	% difference
0.5	2.514	2.464	-2.0
0.7	2.575	2.493	-3.2
0.9	2.520	2.410	-4.4

As shown in Figure 14, convergence is approximately linear with resolution as expected for MH4D.

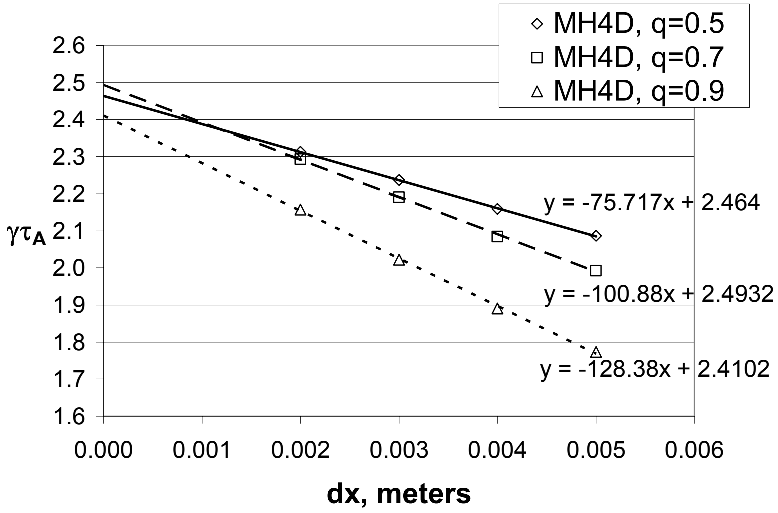

Figure 14: MH4D normalized kinetic energy growth rate predictions vs. resolution. Peak resolution is 2 mm (a/dx=15) which required a total of 350,000 tetrahedra.

Figure 15 shows the kinetic energy evolution of an MH4D simulation. Notice the clear linear behavior beginning at about 0.5 μsec.

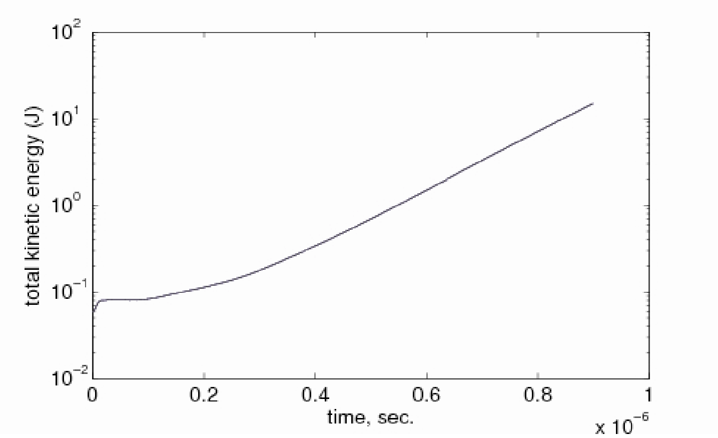

Figure 15: MH4D screw pinch kinetic energy vs. time (dx=5 mm).

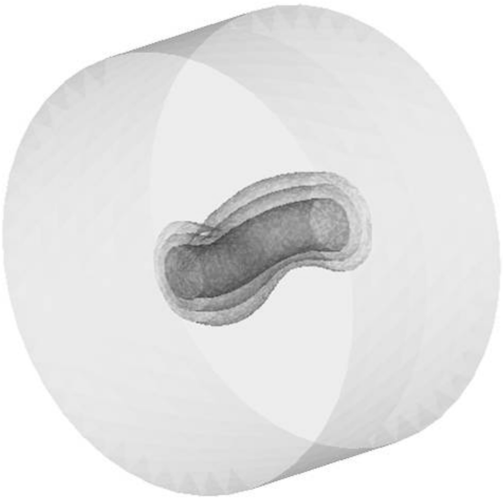

Figure 16: MH4D screw pinch simulation snapshot showing pressure contours. t=0.9 μs (dx=5 mm). For reference, $\tau_A \approx 0.5\mu\mathrm{s}$.

A snapshot of a kinking screw pinch is shown in Figure 16.

As seen in Figure 14, the highest resolution used is 2 mm. With this resolution, there are 15 grid cells across the pinch radius. Higher resolutions are possible, but would not likely alter the conclusions that can be drawn. MH4D simulations agree with linear stability analysis within 5%, and build confidence that MH4D properly captures magnetohydrodynamic plasma behavior. The cause of the 5% discrepancy is not known with certainty. A possible explanation is that non-linear effects are present by the time clear linear growth is present in the simulations.

4.2 Spheromak

In a second linear stability test, the *m*=1 tilt mode of a spheromak in a "tuna can" cylindrical domain was simulated and compared to published growth rate calculations. This test was performed for two main reasons. First, due to the discrepancy between MH4D screw pinch kink mode growth rate predictions and linear stability analyzer predictions, a second benchmark was desirable. Second, the PSI-Center had previously used spheromak tilt mode simulations to test atomic physics models. Developing spheromak tilt simulations in MH4D provided continuity between MH4D atomic physics development and previous atomic physics work.

4.2.1 Theoretical Background

Details about spheromak equilibria can be found in Bellan [12]. The three components of magnetic field for an *m*=0 cylindrical equilibrium are as follows:

$$\begin{aligned} B_r &= -B_0\left(\frac{k_z}{k_r}\right)J_1\left(k_r r\right)\cos\left(k_z z\right) \\ B_\phi &= B_0\sqrt{1+\frac{k_z{}^2}{k_r{}^2}}J_1\left(k_r r\right)\sin\left(k_z z\right) \\ B_z &= B_0 J_0\left(k_r r\right)\sin\left(k_z z\right) \end{aligned} \tag{52}$$

where $k_z=\pi/L$, $k_r=3.8317/R$, and L and R are the length and radius of the cylindrical domain.

Two spheromaks are shown in Figure 17. On the left is a stable spheromak in an oblate or “tuna can” flux conserver. On the right is an unstable spheromak in an prolate flux conserver. The tilt instability can be explained by a minimum energy argument. When L/R is <1.67, as for the tuna can flux conserver, energy is required to tilt the spheromak. When L/R >1.67, a tilted configuration is energetically favorable.

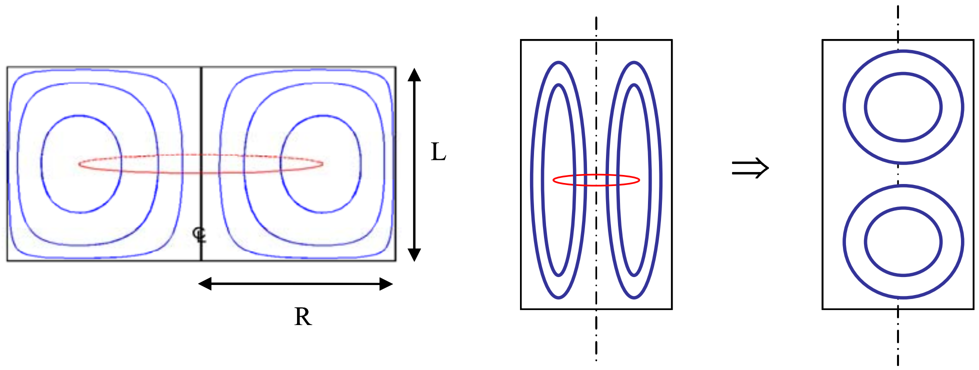

Figure 17: Illustrations of tilt-stable (left) and tilt-unstable (right) spheromak configurations.

Figure 18 shows growth rates versus L/R for various β values.

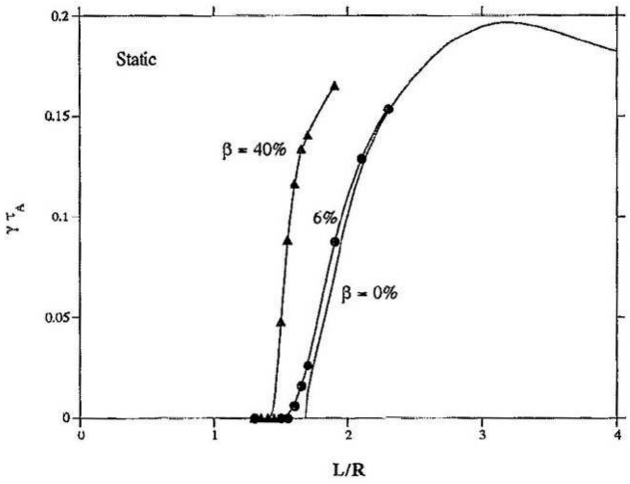

Figure 18: Spheromak *m*=1 tilt growth rates vs. L/R at various β [17].

4.2.2 MH4D modeling of the spheromak

Initially, the plasma has uniform pressure=100 Pa and temperature=10 eV. The initial magnetic field peaks at 1 T, and corresponds to the zero-β equilibrium field per Eqn. (52). Thus, the initial plasma β is 0.025%[7]. L/R=2.5 was chosen for these simulations, where L=2.5 m and R=1 m.

In MH4D, the initial condition must be provided in terms of **A** (MH4D's primitive variable) rather than **B**. For this axisymmetric configuration, we know that

$$\begin{aligned}
\left(\nabla\times\mathbf{A}\right)_r &= \mathbf{B}_r = -\frac{\partial}{\partial z}A_\phi \\
\left(\nabla\times\mathbf{A}\right)_\phi &= \mathbf{B}_\phi = \frac{\partial}{\partial z}A_r - \frac{\partial}{\partial r}A_z \\
\left(\nabla\times\mathbf{A}\right)_z &= \mathbf{B}_z = \frac{1}{r}\frac{\partial}{\partial r}\left(rA_\phi\right)
\end{aligned} \tag{53}$$

Solving the upper equation of Eqns. (53), $A_\phi = -\int_z B_r dz$. One of the two remaining components, A_r and A_z, can be assumed equal to zero. Taking A_z=0, straightforward integration yields a form for **A** whose curl is the desired **B**.

Conducting boundary conditions are used for this problem. Corners at the top and bottom of the cylindrical domain are treated specially. Surface normals are pointed in a direction that is normal to neither of the surfaces that converge at the corners as shown in Figure 19. A special routine in setbc.f is used to ensure

[7] This β value (β=0.025%) is for a uniform pressure profile. The β values shown in Figure 18 are for a non-uniform pressure. With uniform pressure, it is found that β affects growth rates significantly – much more than indicated in Figure 18.

that appropriate normal or tangential components are zeroed on both converging surfaces.

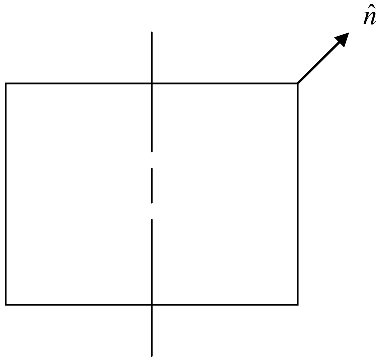

Figure 19: Incorrect surface normal at corner of cylindrical spheromak domain.

Tangential boundary components of **A**, determined from Eqns. (53), are non-zero. With some slight code modifications, MH4D handles this naturally by requiring $\frac{\partial \mathbf{A}_{\text{tang.}}}{\partial t} = 0$ instead of $\mathbf{A}_{\text{tang.}} = 0$ on conducting boundaries.

The perturbation for the problem is a rigid rotor velocity perturbation modulated by parabolic functions of radius and height to prevent perturbed velocity at radial and axial boundaries. The rotation is around an axis perpendicular to the cylinder centerline through the geometric center of the cylinder. The perturbation value is $v = 0.001 v_A$. The Alfvén speed used for this perturbation (and for growth rate normalization, below) is based on the peak magnetic field strength and the uniform initial plasma density.

4.2.3 Results and Discussion

A plot of normalized kinetic energy growth rate versus simulation resolution is provided in Figure 20. A snapshot of a simulated tilting spheromak which is entering the non-linear growth phase is provided in Figure 21.

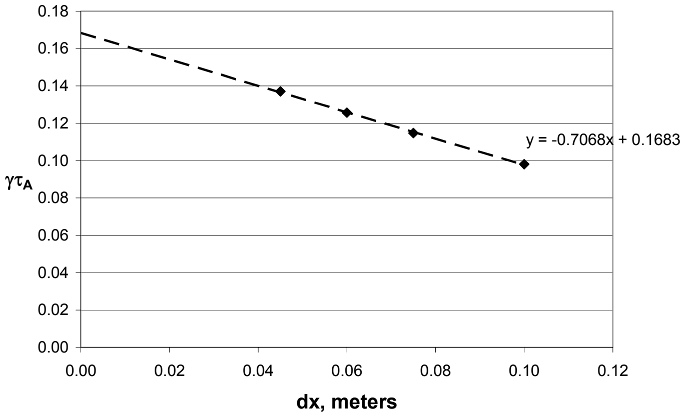

Figure 20: MH4D spheromak normalized kinetic energy growth rates vs. resolution. Peak resolution is dx=4.5 mm (R/dx=25) which required a total of 810,000 tetrahedra.

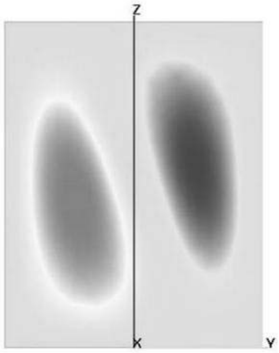

Figure 21: MH4D spheromak tilt simulation, toroidal magnetic field contours. t=32 μsec, dx=10 cm (R/dx=10).

If the tilt is in a known plane, the toroidal field is easily plotted. For example, if the spheromak tilts the y-z plane, the B_x component is the toroidal component (as in Figure 21). In these simulations, it was discovered that grid error can overwhelm the initial perturbation and cause the spheromak to tilt arbitrarily. If the mesh for the spheromak problem is created with T3D by discretizing the entire cylindrical volume at once, grid errors can be asymmetric. To prevent this problem, a grid can be created by reflecting a lengthwise slice. Then, net grid errors are symmetric and the tilt direction is determined by the perturbation.

As seen in Figure 20, the converged growth rate prediction is 0.168. As in the screw pinch simulations, the convergence seen in Figure 20 is linear with resolution. Based on the data in Figure 18, a growth rate of 0.17 is expected for L/R=2.5. Thus the difference between MH4D kinetic energy growth rate prediction and the linear stability prediction is around 1%.

The spheromak tilt results indicate reasonable performance of MH4D.

Chapter 5

ATOMIC PHYSICS TESTS

5.1 Simulation of stationary, constant temperature plasma

Three test problems involving stationary, constant temperature plasma have been solved. Two of the problems have analytical solutions. The third problem is a coronal equilibrium test for which empirical results are available in literature. The test problems and results are presented, and then implementation details are discussed.

5.1.1 Background for analytical test problems

With the ionization and recombination models described in Section 3.5, two simple problems with analytical solutions have been solved with MH4D. In these problems, the plasma has zero velocity, and temperature is constant. A spatially and temporally constant neutral density is assumed. A box domain with coarse discretization (roughly 100 tetrahedra) is used. Conducting hardwall boundary conditions are used.

The equation describing ionization is

$$\frac{\partial \rho_i}{\partial t} = \langle \sigma_{ion} \mathbf{v}_e \rangle \rho_i n_n ,$$

which has the analytical solution,

$$\rho_i\left(t\right) = \rho_0 \exp\left[\langle \sigma_{ion} \mathbf{v}_e \rangle t\right],$$

where ρ_0 is the initial plasma density. For recombination,

$$\frac{\partial \rho_i}{\partial t} = -\langle \sigma_{rec} \mathbf{v}_e \rangle \rho_i n_i = -\langle \sigma_{rec} \mathbf{v}_e \rangle \rho_i^{\,2} C\,,$$

where C is the conversion from kg/m^3 to #/m^3. This has the solution,

$$\rho_i = \left(t\langle \sigma_{ion} \mathbf{v}_e \rangle C + \frac{1}{\rho_0} \right)^{-1}.$$

These two analytical problems are called the "isolated ionization" and "isolated recombination" problems.

5.1.2 Background for coronal equilibrium test problem

At a given temperature, the ionization fraction of a plasma in coronal equilibrium is predictable. A variable neutral density is implemented in MH4D to allow this test.

5.1.3 Results and discussion

MH4D successfully produces the analytical solutions for various initial data and ionization and recombination rates for the isolated ionization and isolated recombination problems. Some difficulty was encountered with timestep choice in the isolated ionization problem. Consider the number density change for plasma, $\frac{\partial n_i}{\partial t} = \langle \sigma_{ion} \mathbf{v}_e \rangle n_i n_n$. MH4D is set up so that the number of new ions cannot exceed the number of available neutrals. Thus, if $\frac{\partial n_i}{\partial t} \Delta t$ exceeds n_n, the solution found by MH4D does not match the analytical solution (this is obvious in retrospect).

MH4D predicts coronal equilibrium ionization fractions similar to those estimated in Goldston and Rutherford [9] as shown in Table 3.

Table 3: MH4D coronal equilibrium predictions compared to literature.

T_{eV}	% ionized, MH4D	% ionized, Goldston and Rutherford
13.6	99.997	~99.999
1.5	57	~50

There is an obvious theoretical timestep limit for ionization and recombination rates,

$$dn_i = \frac{\partial n_i}{\partial t}\Delta t < n_n \quad \text{and} \quad dn_n = \frac{\partial n_n}{\partial t}\Delta t < n_i .$$

These limits reflect the fact that the number of new ions cannot exceed the number of existing neutrals and *vice versa.* In addition to this theoretical limit, a practical limit exists. If $dn_{i,n}$ $(= \frac{\partial n_{i,n}}{\partial t}\Delta t)$ is of order $n_{i,n}$, oscillatory solutions are obtained for the coronal equilibrium problem as shown in Figure 22. Restricting Δt such that $dn_{i,n} < \frac{n_{i,n}}{10}$ is observed to produce temporally smooth solutions.

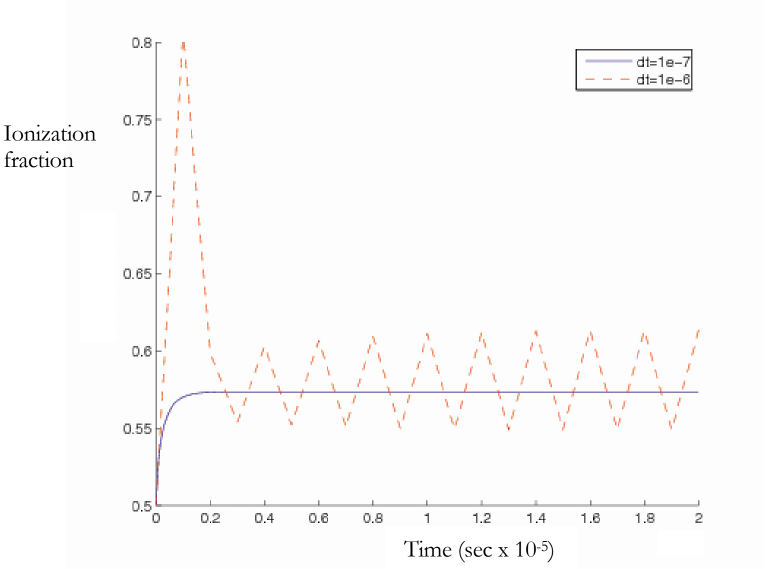

Figure 22: Atomic physics simulation ionization fraction vs. time at 1.5 eV. With dt=1x10^{-7}, the solution is smooth. With dt=1x10^{-6}, the solution is oscillatory.

5.2 Spheromak tilt with neutral gas

A spheromak tilt problem has been used to qualitatively verify the modifications to the momentum and pressure equations seen in Eqns. (45) and (46). There are no standard test problems to assess a code's ability to capture atomic physics effects. However, when a plasma is increasing its mass by ionizing a neutral gas background, the atomic physics terms in the momentum equation should slow any instability growth rates. The spheromak tilt mode is simulated with and without an ionizing neutral gas background. Generally, if plasma mass increases significantly, a significant slowing of the growth rate is expected.

5.2.1 Spheromak tilt test problem background

General theoretical background and implementation details of the spheromak problem setup can be found in Section 4.2. In this atomic physics test, β=0.25% is used. This corresponds to T=100 eV. In the spheromak tilt benchmark test described in Section 4.2, T=10 eV is used. The higher temperature, 100 eV, is desirable for this atomic physics test because it causes full ionization prior to the linear kinetic energy growth phase (but the associated higher β does slightly reduce the growth rate as the results indicate).

5.2.2 Results and discussion

Figure 23 shows results kinetic energy vs. time for a spheromak tilt simulation in which a background neutral gas is initialized with 1/5 the density of the initial plasma.

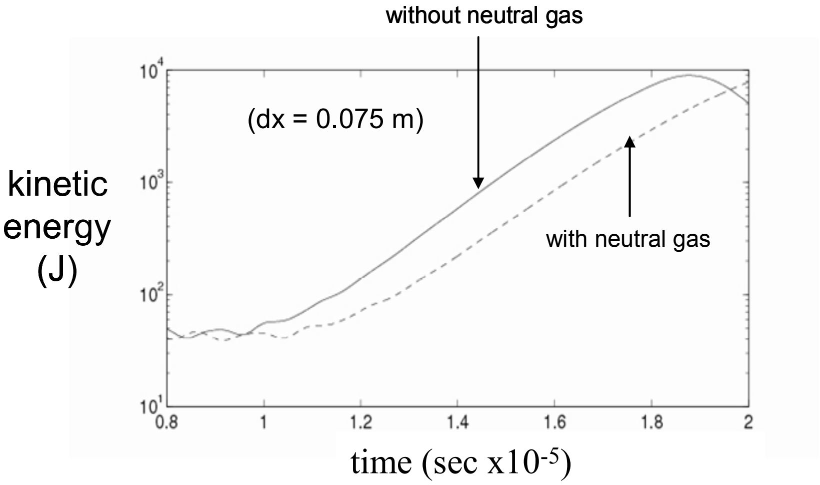

Figure 23: Kinetic energy vs. time from spheromak tilt simulations with and without atomic physics. Growth rate is clearly reduced in simulation with initial neutral gas.

Figure 24 shows how the total plasma mass varies with time. As seen, the neutral gas is quickly and nearly completely ionized. The increased mass slows the spheromak tilt as seen in Figure 23. The converged tilt growth rate without neutral gas is found to be 0.161. With an initial neutral gas background, the growth rate is 0.146 – reduced by 9%. This result qualitatively verifies the atomic physics implementation.

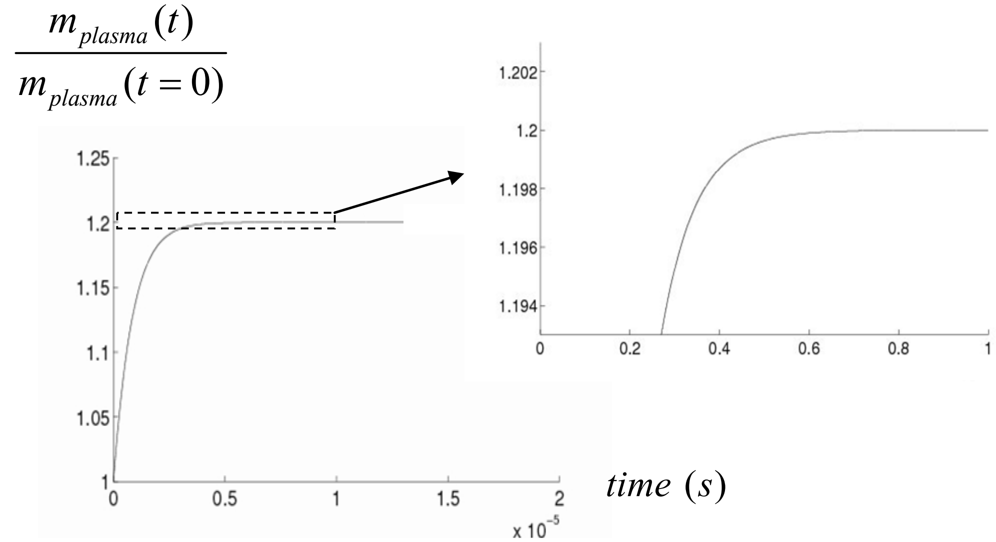

Figure 24: Total plasma mass as a fraction of initial mass vs. simulation time for spheromak with initial neutral gas. The plasma is fully ionized by 10 μs.

Chapter 6

DEVELOPMENT BY APPLICATION TO THE ZAP FLOW Z-PINCH EXPERIMENT

Since the ultimate goal of computational plasma science is to understand phenomena observed in experiment, an important part of code development is application to experiments. This aspect of MH4D development has focused on the ZaP Flow Z-Pinch Experiment at the University of Washington [32]. MACH2 [33] ZaP simulation results are used as a benchmark for the MH4D simulations.

6.1 Introduction to the ZaP Experiment and terminology

A ZaP schematic is provided in Figure 25. As indicated, the annular region between the inner and outer electrode is called the "acceleration region". The cylindrical region beyond the tip of the inner electrode is called the "assembly region". Other important features include the neutral gas injection plane and the hole in the endwall that allows outflow.

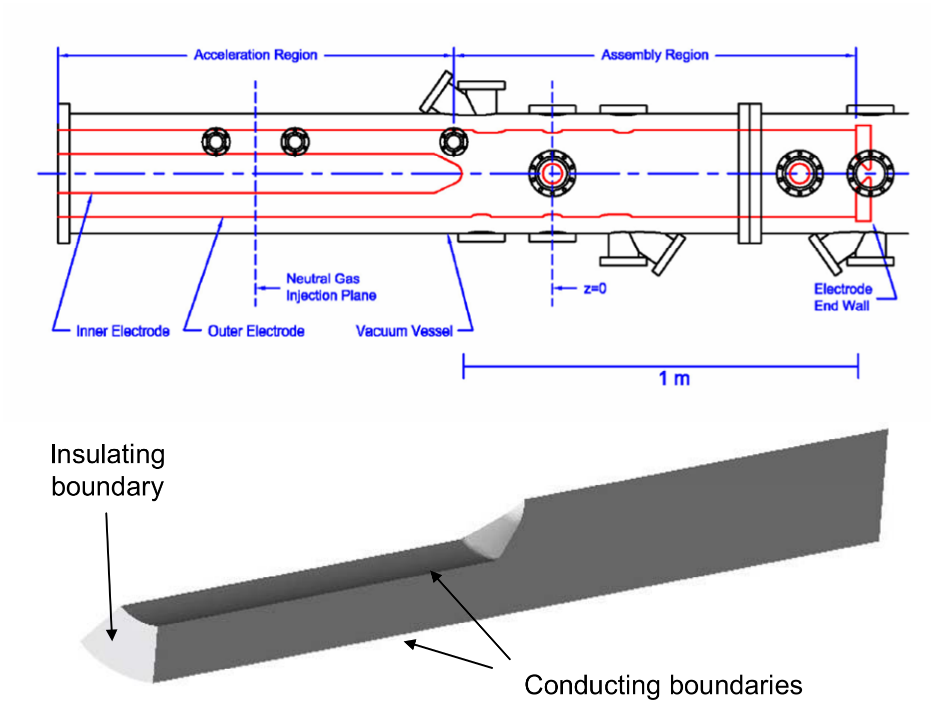

Figure 25: ZaP simulation diagram and MH4D 1/8-slice domain. An azimuthal magnetic field with 1/r dependence is applied at the insulating boundary indicated.

In ZaP, neutral gas (often Hydrogen) is injected into the acceleration region, the gas is ionized and accelerated into the assembly region where a Z-pinch with sheared axial flow is formed. This process is depicted in Figure 26.

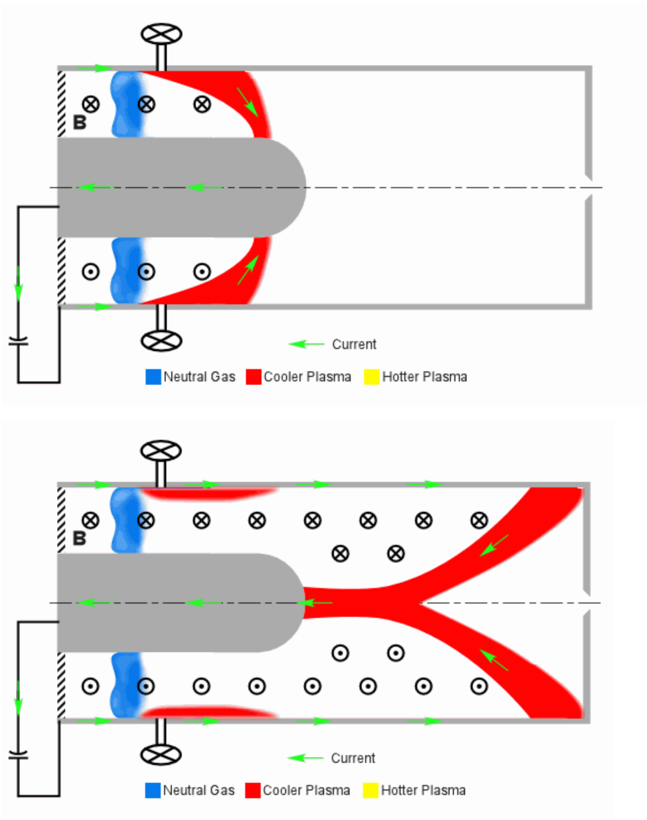

Figure 26: Conceptual diagrams of ZaP Z-pinch formation [34]. In the upper frame, an annular current sheet has developed and a "snowplow" effect is seen. In the lower frame, the Z-pinch formation has started and residual neutral gas and plasma is present in the acceleration region.

While the neutral gas is still concentrated near the ports, voltage is applied and some of the gas is ionized. This ionized gas forms an annular current sheet which is accelerated axially into the assembly region by Lorentz forces. Near the inner electrode, higher current density and higher magnetic fields cause a "snowplow" effect in which plasma close to the inner electrode moves faster than outer plasma. The sheet is stretched as it forms the Z-pinch, embedding axially sheared flow in the pinch. Some residual plasma is left behind in the acceleration region. New plasma is formed from the neutral gas that was not initially ionized. Sheared flow is probably maintained to some extent by plasma that emerges from the acceleration region well after initial pinch formation. Sheared flow stabilizes the Z-pinch for over 2000 times the growth time of a static Z-pinch [32]. Resolved MHD simulations of ZaP should capture the essential behavior described above.

6.2 Basic ZaP simulation approach

1-eV plasma is initialized in an annular volume with 20 cm axial length, centered on the neutral gas injection plane in the acceleration region. The initial plasma density is 6.0x10^{-5} kg/m^3, corresponding to a total mass of 2.8x10^{-7} kg. Total mass injected in the experiment is typically 1-3x10^{-7} kg.

Flux is injected at the insulating boundary shown in Figure 25[8]. To accomplish the flux injection, a time-varying magnetic field boundary condition is applied to the insulating back wall. The applied field is in the azimuthal direction. The current generated due to the applied field can be calculated using Ampère's Law: $B_\theta = \mu_0 I_{enc} / \left(2\pi r\right)$. (Refer to Figure 28 for current profiles used in simulations.)

Except for the insulator, boundaries are modeled as conducting walls. To make high-resolution simulations feasible, periodic boundary conditions are used to model only a 1/8-slice of the domain. Various combinations of Chodura and Spitzer resistivity are used. Sometimes, a resistivity floor is used to maintain dissipation in the simulations. A resistivity cap is always used to prevent extreme numerical stiffness. A density floor is used with a value 10 to 100 times smaller than the initial density in the gas puff.

[8] Treating the entire back wall of the experiment as an insulating boundary is a simplification, but modeling the more complicated insulator geometry should not significantly change the simulation results.

6.3 Assessment of implicit induction advance via ZaP simulation

As described in Section 2.4, the explicit timestep limit for the induction equation is prohibitive. By advancing the induction equation implicitly, presumably, significantly larger timesteps can be taken and computational effort can be dramatically reduced for a given simulation without sacrificing accuracy. This expectation has been tested via simulations of the ZaP acceleration region. This section presents several implicit runs and one explicit run with different timestep sizes, but with a fixed computational grid and fixed simulation parameters. The peak resistivity for these simulations is 0.025 ohm-m (equivalent to Spitzer resistivity for a 0.1 eV plasma). A combination of Spitzer and Chodura resistivity is used. The density floor is 1x10^{-6}. The mesh size is 6 mm. In Table 4, key simulation characteristics of these runs are shown for each timestep size. Figure 27 gives a plot of computational effort versus timestep size.

Table 4: Implicit advance accuracy with various timestep sizes. Key simulation characteristics are shown. There is <1% variation in maximum velocity or location of the peak pressure. The peak pressure value increases by only 4% for the largest timestep.

dt (ns)	v_{max} (m/s)	*deviation (%)*	p_{peak} (Pa)	*deviation (%)*	z-location of p_{peak} (m from insul. boundary)	*deviation (%)*
0.06*	65410	*0.000*	320686	*0.000*	0.36152	*0.000*
0.5	65440	*0.046*	321986	*0.405*	0.36152	*0.000*
1	65460	*0.076*	323857	*0.989*	0.36152	*0.000*
2	65520	*0.168*	326575	*1.836*	0.36322	*0.470*
4	65610	*0.306*	334595	*4.337*	0.36152	*0.000*

* Explicit

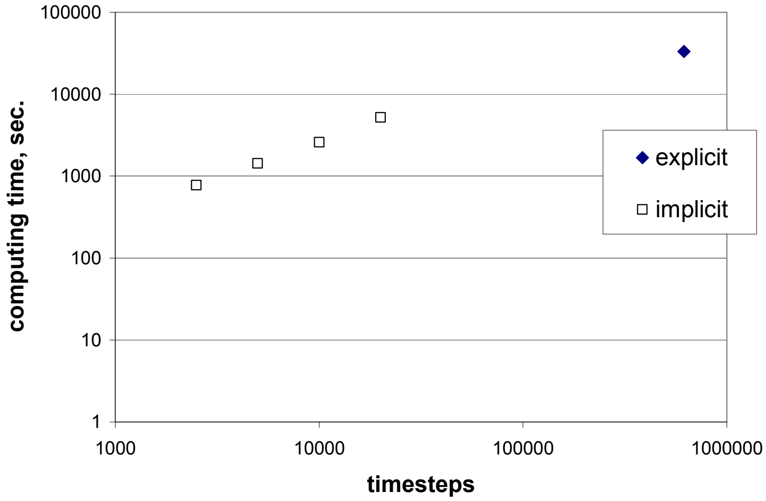

Figure 27: Computational effort with implicit induction advance. Computing time vs. number of timesteps is shown for the five runs in Table 4. Computing time is reduced linearly with the number of timesteps for the runs shown.

The qualitative plasma behavior in all of these simulations is identical. The deviation of 4% in pressure, seen in Table 4, certainly does not obscure the essential plasma behavior. The results shown in Figure 27 suggest that increasing the timestep has not yet become counterproductive (with a sufficiently large timestep, the benefit of less time steps would be balanced by time spent in the iterative solver). The maximum timestep for these simulations, 4 ns, is dictated by the wave-flow timestep limit (see Section 2.5). These results indicate that pushing the timestep to the wave-flow timestep limit is generally acceptable and appropriate for maximizing computational efficiency.

6.4 MACH2 benchmark

MH4D ZaP simulations have been performed. The results are benchmarked against ZaP simulation results from MACH2 [33], a 2½D MHD code. The MACH2 simulations were not conducted as part of this research.

In Section 6.4.1, MACH2 and MH4D simulation conditions are compared. Sections 6.4.2 and 6.4.3 present MACH2 and MH4D results. In Section 6.4.4, results are compared and discussed.

6.4.1 Simulation conditions

Simulation conditions for MACH2 and MH4D are shown in Table 5. In ZaP, a hole in the endwall allows outflow. This outflow boundary is modeled in MACH2 but not in MH4D. The resolutions used in the MH4D runs are significantly lower than the corresponding resolutions in MACH2 runs. Differences in density floor and radiation modeling are probably of secondary importance as compared to the outflow boundary condition and the resolution difference.

The current profiles for MH4D and MACH2 are similar as shown in Figure 28.

Table 5: Comparison of ZaP simulation conditions for MACH2 and MH4D. Differences are highlighted. Conditions for MH4D runs at two resolutions (coarse and fine) are shown. MACH2 uses elongated rectangular cells (with length dimension dz larger than radial dimension dr). In the assembly region, resolution is maximum on the pinch axis and minimum at the radial wall.

Feature	**MACH2**	**MH4D**
Current b.c.	See Figure 28.	Similar. See Figure 28.
Outflow b.c.	Yes	No
$T_{init.}$	1 eV	1 eV
$\rho_{init.}$	6e-5 kg/m^3	6e-5 kg/m^3
$\rho_{\mathbf{floor}}$	1e-8 kg/m^3	1e-6 / 7 kg/m^3 (coarse / fine)
Radiation	Line radiation, 1% O_2	None
Resistivity	Spitzer	Spitzer
Ohmic heating	Yes	Yes
$(\nabla p)_n = 0$	Yes	Yes
Velocity b.c.	Slip	Slip
Resolution in accel. region	dr=2.5 mm, dz=4 mm	dx_{fine} = 4 mm dx_{coarse} = 6 mm

Resolution in assembly region (pinch axis / wall)	dr = 0.5 / 3 mm
	dz =4 mm
		dx_{fine} = 2 / 4 mm
		dx_{coarse} = 3 / 6 mm

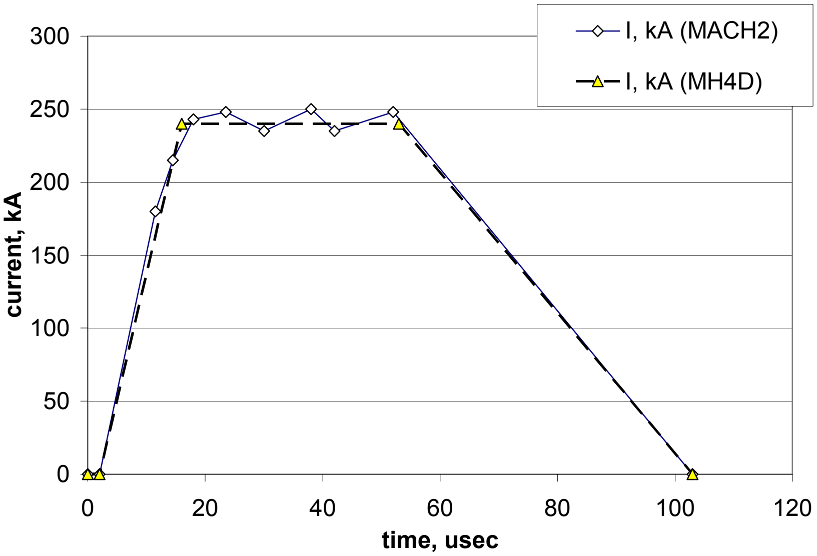

Figure 28: Current profiles for MH4D and MACH2 ZaP simulations. The MH4D applied current profile closely matches the MACH2 profile.

6.4.2 MACH2 results

Snapshots of density and pressure during a MACH2 simulation are presented in Figure 29 and Figure 30. Figure 29 concentrates on the first 15 μs on the acceleration process, while Figure 30 shows snapshots from 20 to 50 μs. The MACH2 simulation continues through 100 μs but these snapshots illustrate the key predicted plasma behavior.

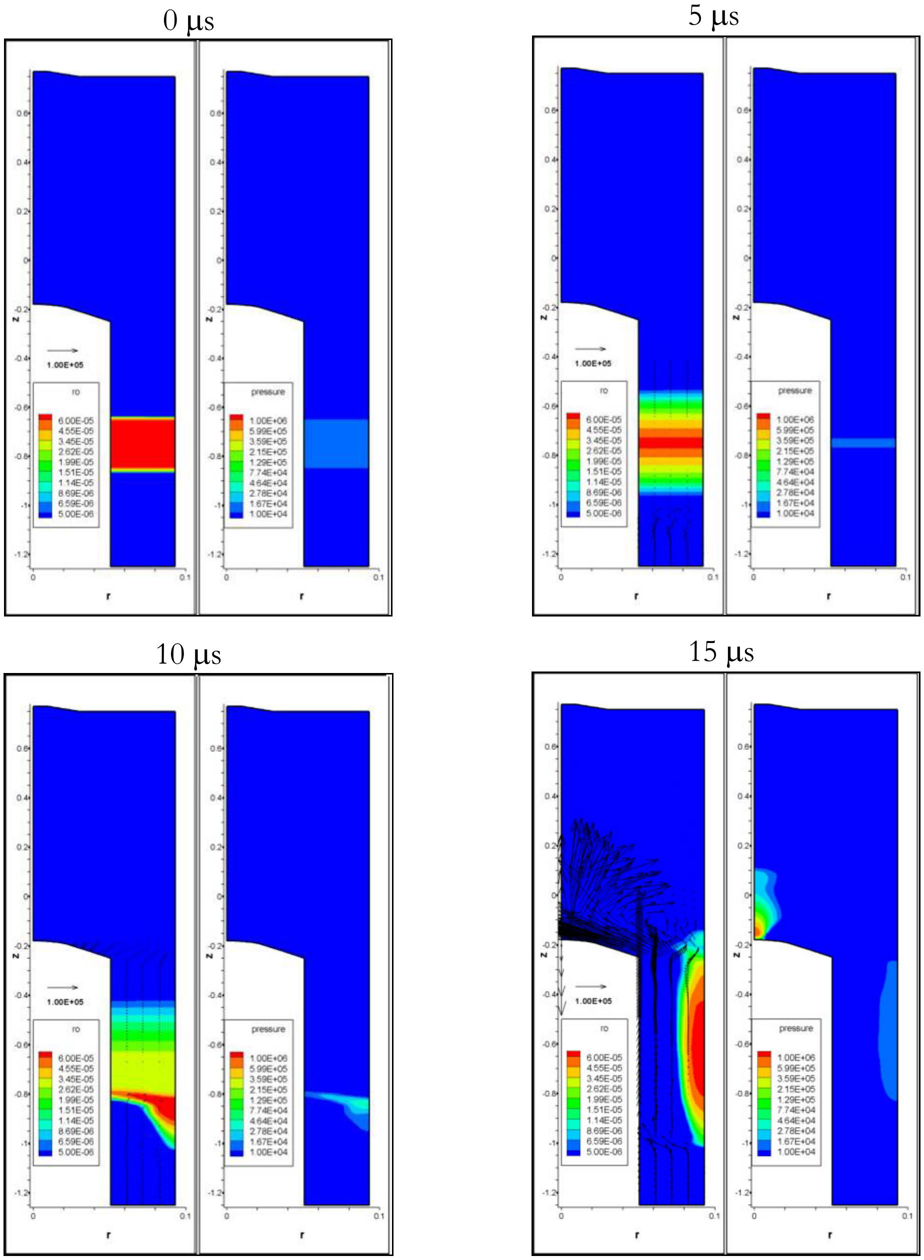

0 μs

5 μs

10 μs

15 μs

Figure 29: Snapshots of MACH2 ZaP simulation acceleration behavior. The snowplow effect pushes plasma to the outer wall. Pinch formation begins at 15 μs. (z-axis scale is compressed 5:1 relative to the radial scale.)

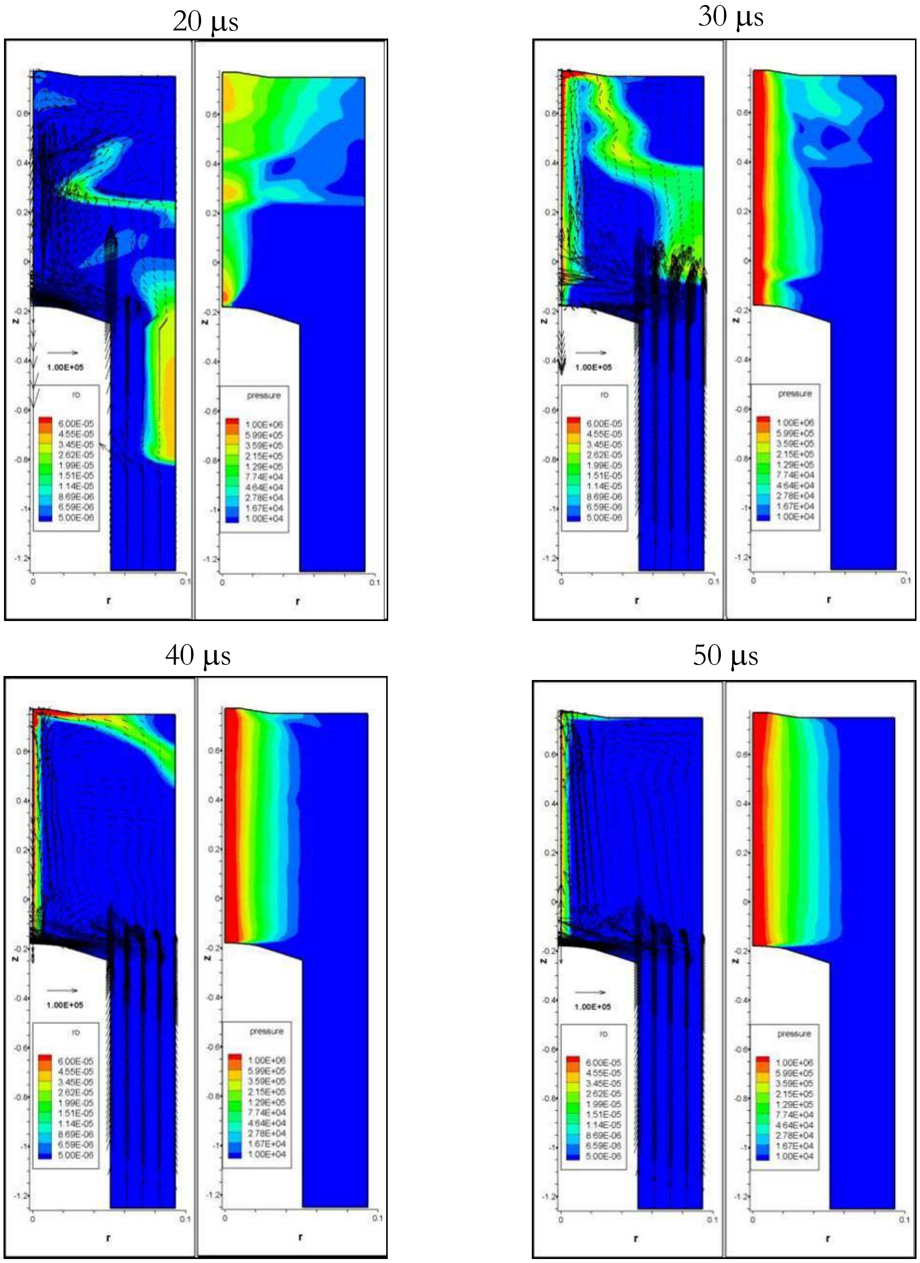

Figure 30: Snapshots of MACH2 ZaP simulation assembly behavior. Plasma from the acceleration region feeds the pinch and is incorporated in the pinch or exhausted through the outflow boundary. (z-axis scale is compressed 5:1 relative to the radial scale.)

6.4.3 MH4D results

Two MH4D simulations are presented. Parameters for the simulations are shown in Table 5. One is called the “coarse” simulation and the other, “fine”. The coarse simulation has 420,000 tetrahedra and the fine simulation has 1,300,000 tetrahedra. The differences in the simulations are in resolution and density floor: in the “fine” run, mesh size 50% smaller, and the density floor is lower by a factor of 10. Snapshots corresponding to the snapshots presented for MACH2 are presented in Figure 31 and Figure 32 for the coarse run and Figure 33 and Figure 34 for the fine run.

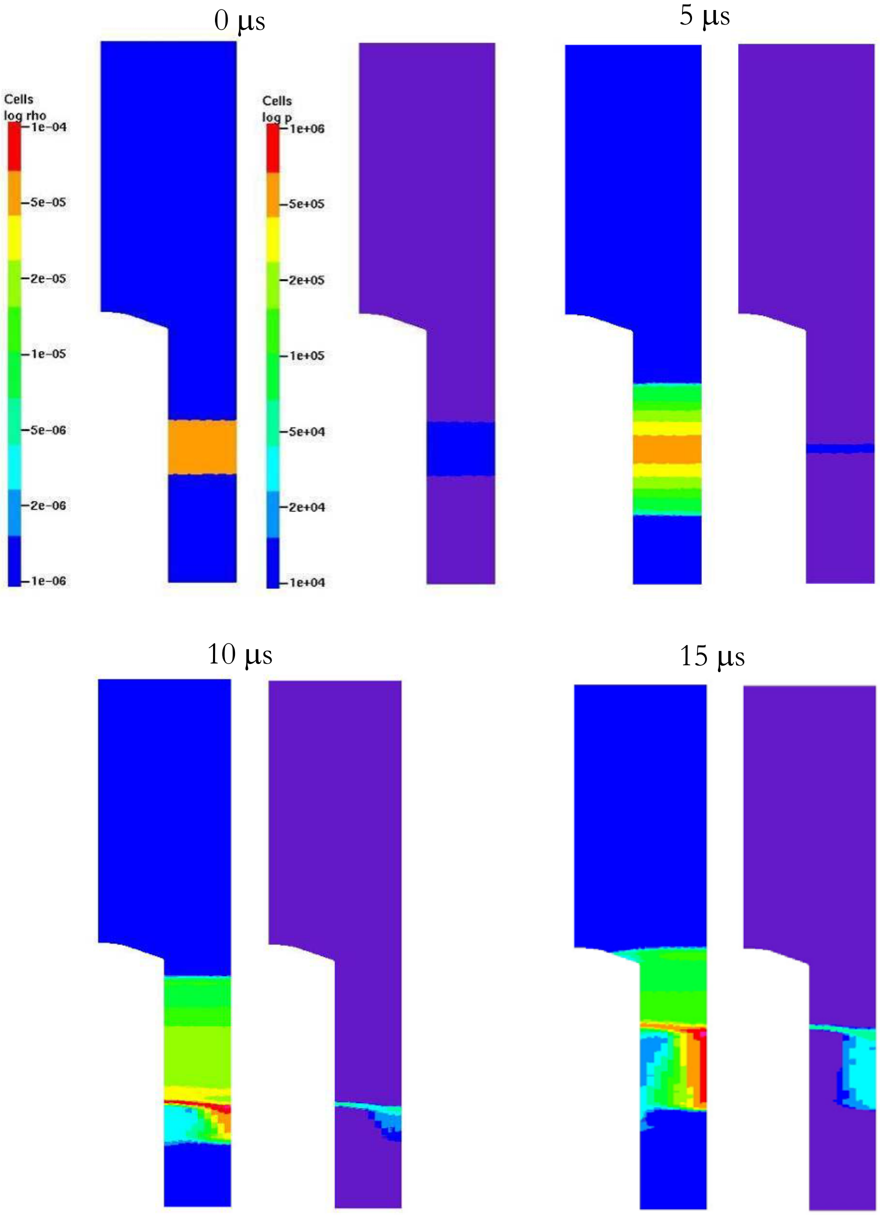

Figure 31: Snapshots of "coarse" MH4D ZaP simulation acceleration behavior. Snowplow only partially forms and plasma is almost uniformly accelerated axially. (z-axis scale is compressed 5:1 relative to the radial scale.)

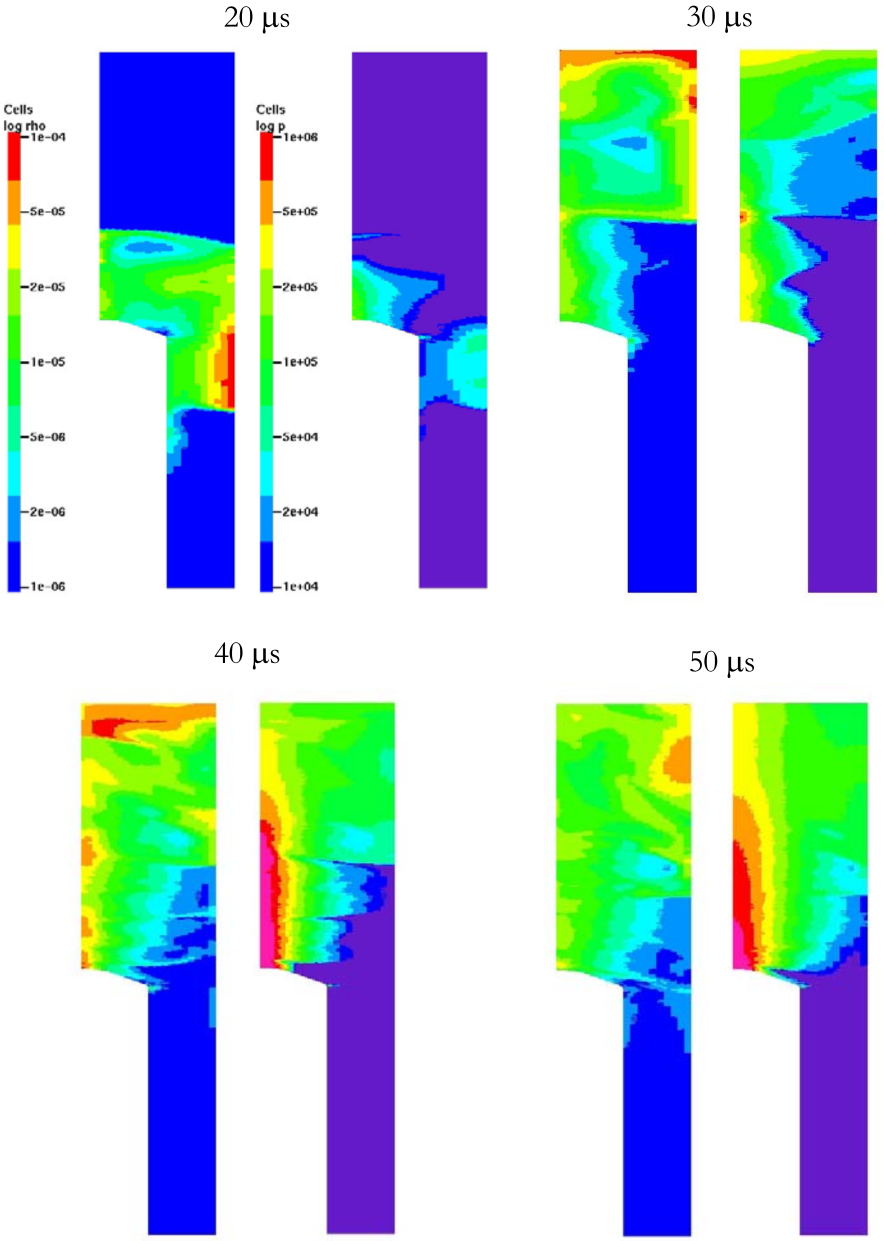

Figure 32: Snapshots of "coarse" MH4D ZaP simulation assembly behavior. Uniformly accelerated plasma compresses and rebounds from the endwall, creating shock waves in the simulation. (z-axis scale is compressed 5:1 relative to the radial scale.)

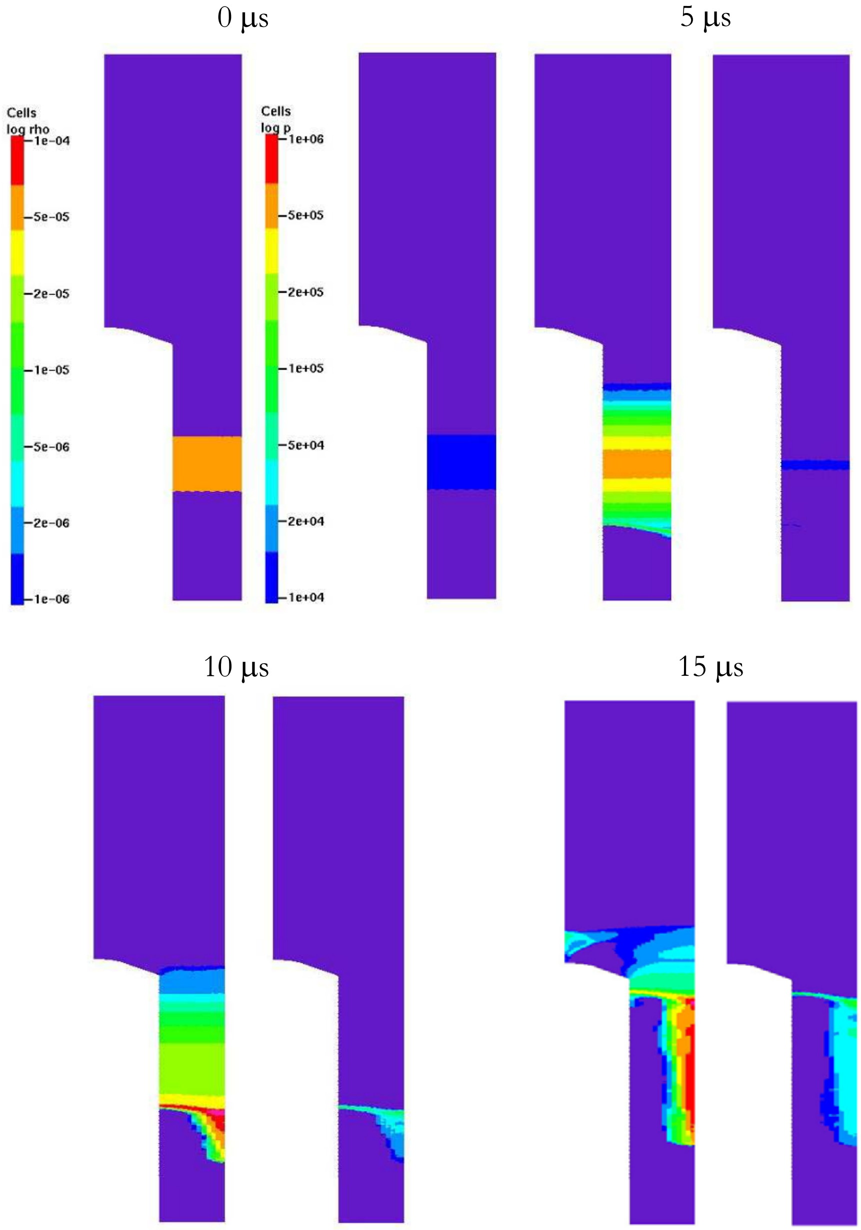

Figure 33: Snapshots of "fine" MH4D ZaP simulation acceleration behavior. Snowplow forms and pushes plasma to outer wall. (z-axis scale is compressed 5:1 relative to the radial scale.)

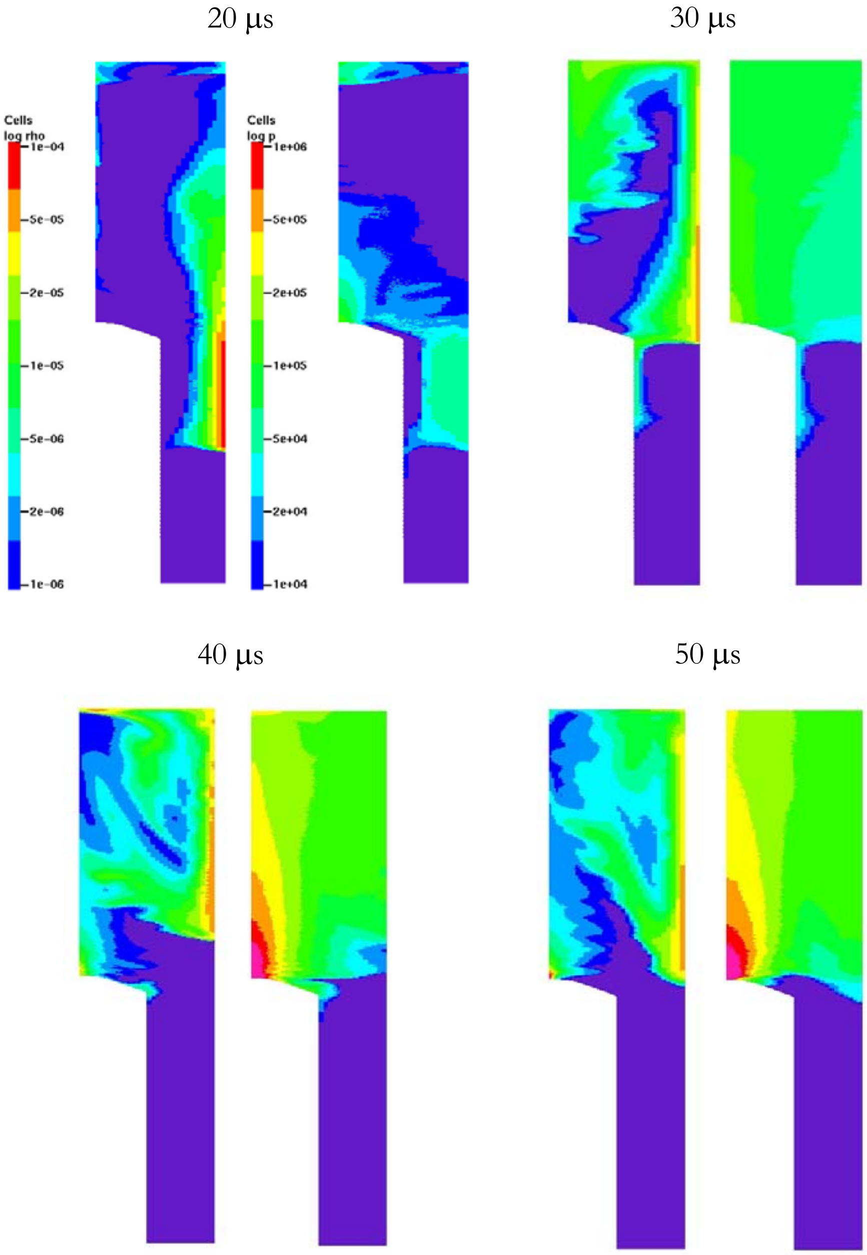

Figure 34: Snapshots of "fine" MH4D ZaP simulation assembly behavior. Plasma was pushed against outer wall and slowly enters assembly region. No density pinch is formed. Pressure pinch is not as tight as in MACH2. (z-axis scale is compressed 5:1 relative to the radial scale.)

6.4.4 Comparison and discussion

The acceleration region behavior in the fine MH4D simulation is much different than in the coarse simulation. In the coarse simulation, the plasma is accelerated almost uniformly toward the assembly region. Inertia carries the bulk of the plasma to the endwall where it rebounds, causing shockwaves that are not seen in the MACH2 results or in the fine simulation results. In the fine simulation, as in MACH2, the snowplow forces the bulk of the plasma to the outer wall where it moves slowly toward the assembly region. Density distributions at 20 and 30 μs in the fine simulation are comparable to those seen in the corresponding MACH2 plots.

ZaP diagnostics reveal a discrete Z-pinch with 1-cm radius. In the 30, 40 and 50 μs snapshots, MACH2 density contours show this 1-cm-radius pinch on the axis. MH4D does not capture this peaked density in either the coarse or the fine simulations. This difference is probably due primarily to insufficient resolution in the pinch region. High radial gradients in pressure and density are not resolved, and a tight pinch cannot form in the simulations. Outflow, which is modeled in the MACH2 simulation, but not in the MH4D simulations, could also play a role.

High magnetic fields are present in the simulations at the cathode nosecone. Increasing resolution at the nosecone reduces the maximum magnetic field magnitudes, indicating that the high fields are at least partly due to numerical error (see discussion of $\nabla \bullet \mathbf{B}$ in Appendix A.3). A "shadowing" effect could also contribute to these high magnetic fields, as the predominantly axially-directed plasma passes the cathode nosecone.

The semi-implicit algorithm is not used in these simulations. Some difficulties have been encountered in applying the algorithm. However, even with the semi-implicit momentum advance functioning to eliminate the magnetosonic wave speed timestep restriction, high flow speeds in ZaP will force small timesteps. In MACH2, this issue is alleviated by using elongated grid cells in the direction of high flow speeds (i.e. the axial direction), easing the timestep restriction. MH4D cannot use this grid alignment technique because distorted tetrahedra cause numerical inaccuracy.

Computational effort for the fine MH4D run was 10 hours on 64 NERSC Bassi processors (1.9 GHz per processor). Using the semi-implicit algorithm, the effort could be reduced by roughly a factor of 5, despite the high flow speeds. Based on this information, a simulation with MACH2-like resolution seems within reach.

In summary, MH4D simulation results are seen to converge to the MACH2 results in the acceleration region. However, predictions by MH4D and MACH2 of Z-pinch behavior in the assembly region differ significantly. As discussed, further research to develop and improve MH4D ZaP simulations is possible. Such research would at least explore and probably extend the known capabilities of the code.

6.5 ZaP simulation with 3D neutral gas injection

To exercise the 3D capability of MH4D, a ZaP acceleration region simulation was performed with a 3D "puff" of neutral gas replacing the previously-described uniform density "block" initial condition. This 3D initial condition is shown in Figure 35.

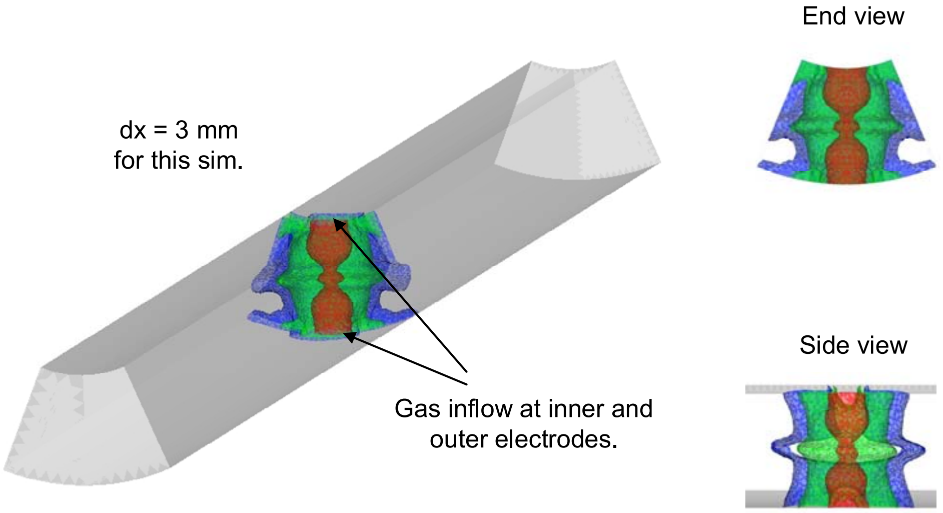

Figure 35: 3D gas "puff" initial condition. This initial condition is generated by separately simulating gas injection. During injection, by not advancing the induction equation, plasma is treated like neutral gas.

Gas injection is accomplished in MH4D by designating inflow boundary vertices and allowing normal velocity, and normal pressure gradients for those vertices. Dirichlet boundary conditions are set on pressure and density. In gas injection simulations (i.e. the simulations to generate the initial condition shown in Figure 35), the induction equation is not advanced and magnetic field and vector potential are zero everywhere in the domain. Density and pressure boundary values and injection time were varied to produce a gas puff with reasonable characteristics. The total injected mass in the initial condition shown in Figure 32 is equal to the total mass in the 2D density block initial conditions used for MACH2 and MH4D simulations shown in Section 6.4.

Figure 36 presents the 3D puff simulation results. To visualize simulated plasma behavior, two cutplanes are used as shown. Density contours in these two cutplanes are shown at several simulation times. The initially azimuthally asymmetric plasma symmetrizes as the plasma is accelerated and as it converges on the pinch axis.

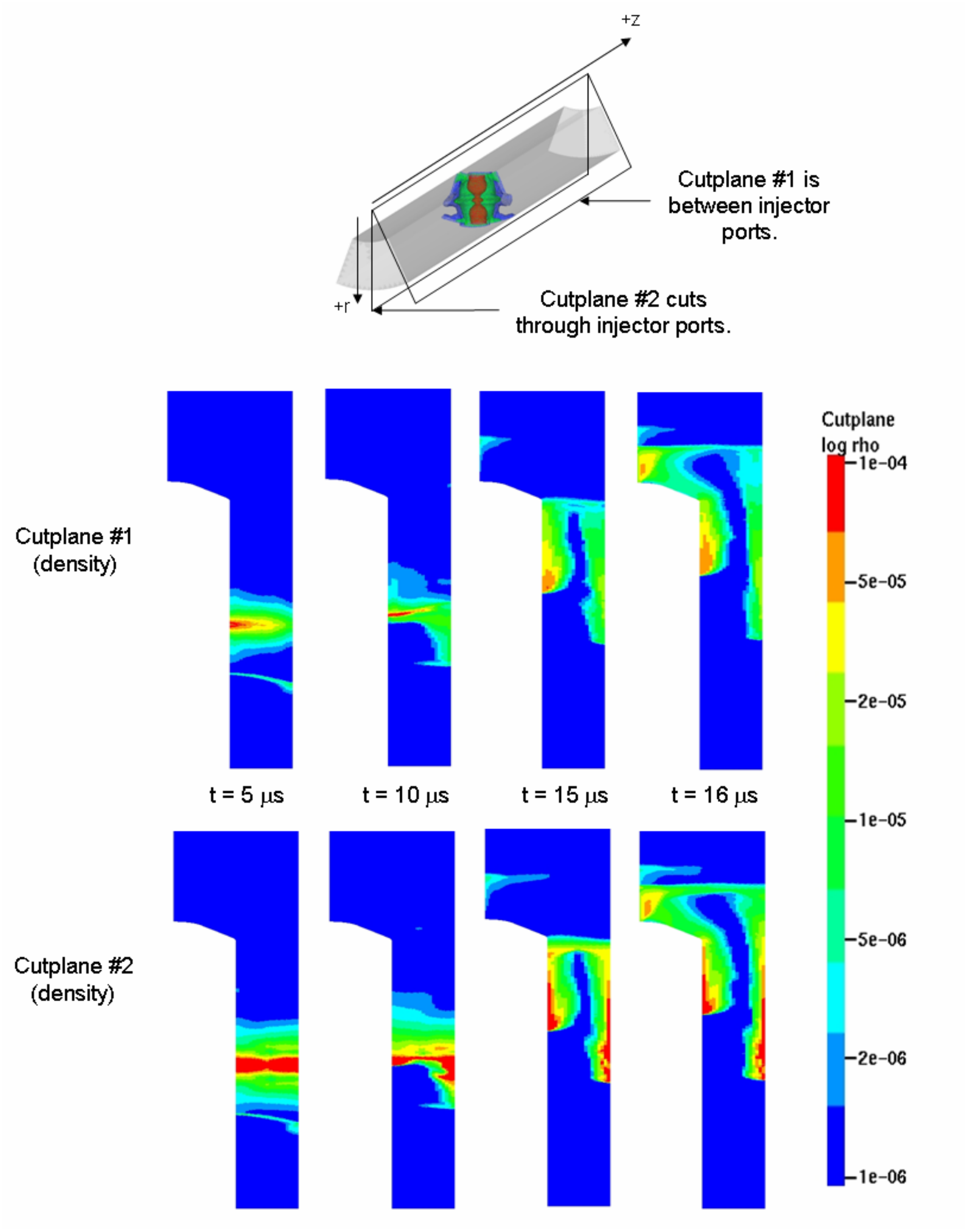

Figure 36: Density evolution in ZaP simulation with 3D gas puff initial condition. At t=0, plasma is azimuthally localized in the injection plane. Significant azimuthal symmetrization is evident as the simulation progresses. (Note that the entire ZaP domain is simulated, but the visualized domain is truncated at approximately 0.2 meters axially beyond the cathode tip.)

Azimuthal symmetrization is also observed experimentally. Figure 37 shows Imacon Fast-Framing Camera pictures taken from the ZaP endwall looking in the negative z direction. Breakdown occurs at a single injection location. The accelerating plasma symmetrizes azimuthally.

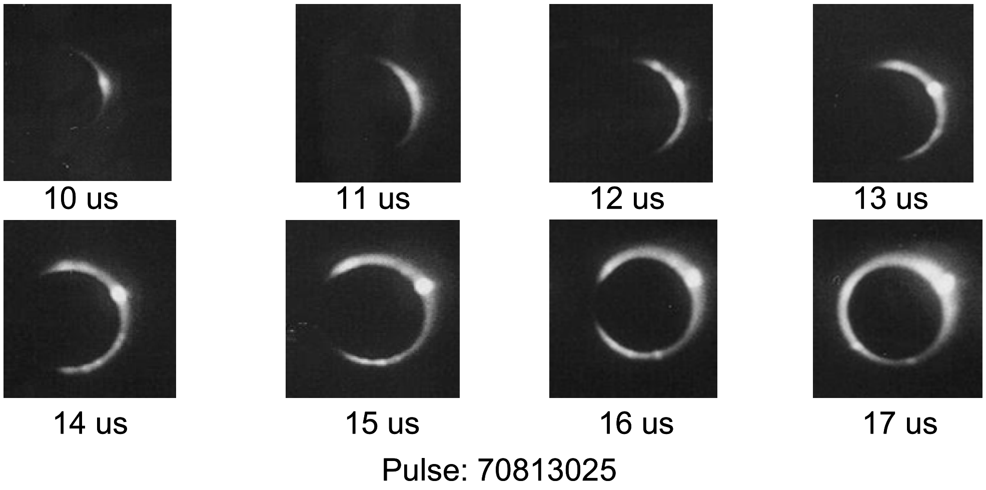

Figure 37: Imacon images looking into the accelerator from the end of ZaP. Breakdown occurs at one of the eight gas ports. The plasma symmetrizes azimuthally as it is accelerated.

6.6 ZaP simulation with atomic physics

The MH4D atomic physics implementation has been applied to ZaP. Plasma and neutral gas are initialized in the acceleration region. The simulations described here begin with an ionization fraction of 1/2. Other simulation parameters are similar to those described in Section 6.3.

Figure 38 shows snapshots of the simulated neutral gas density and plasma density. As seen, a significant part of the original neutral gas is ionized. The simulation is stopped at 15 μs because the plasma collides with the endwall in the acceleration region simulation. Figure 39 shows the neutral gas density vs. time. As shown, net plasma generation occurs throughout the simulation.

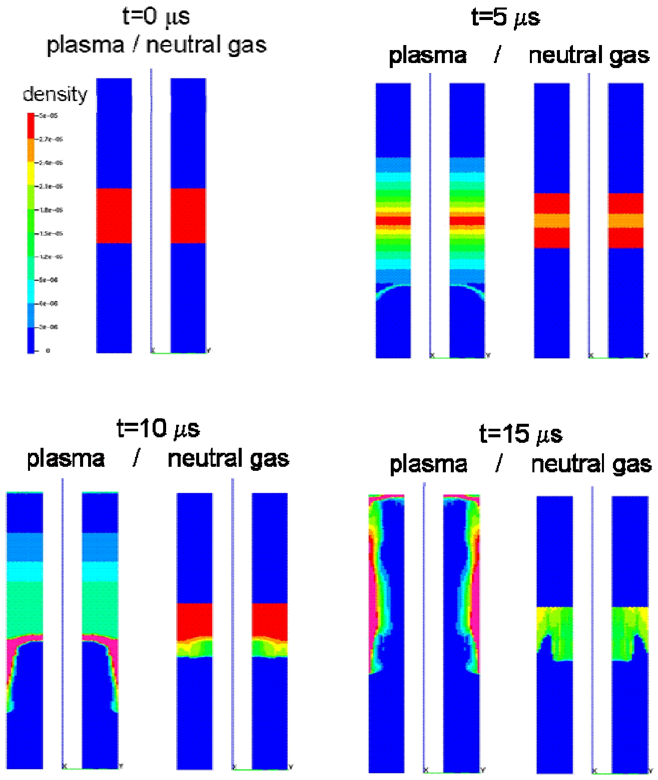

Figure 38: Snapshots of ZaP acceleration region simulation with neutral gas. Simulation is stopped at 15 μs when plasma hits endwall. Neutrals are ionized by hot plasma. (dx=4 mm)

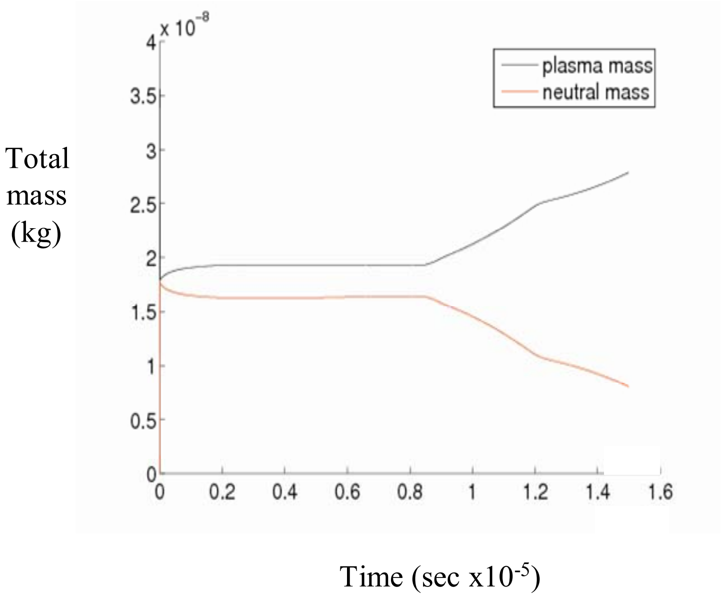

Figure 39: Plasma mass and neutral mass vs. time for acceleration region simulation with neutral gas. Significant plasma generation begins around 9 μs and continues through the simulation.

The atomic physics model implemented in MH4D predicts a source of plasma via neutral gas ionization. As described in Section 6.1, this plasma source likely plays a role in maintaining the sheared axial velocity profile that stabilizes the Z-pinch.

Chapter 7

CONCLUSION

7.1 Concluding remarks

MH4D has been improved as a computational tool by implementing useful boundary conditions for plasma simulation, and by adding important physics features to the code. A periodic boundary condition, useful for domain reduction, mode selection, and wave modeling, is now available. An insulating boundary condition has been implemented and allows flux injection. Spitzer and Chodura resistivity models have been added, and Ohmic heating is now an option. Atomic physics has been implemented. Simulations that have been conducted with atomic physics provide insight into requirements for numerical stability and accuracy, and form a basis for future development in MH4D or other codes.

The quasi-linear regimes of the non-linear screw pinch kink and spheromak tilt instabilities have been simulated with MH4D. The results are benchmarked against linear stability code results, and agreement is reasonable.

MH4D is now adaptable to a variety of problems as shown in this research. In addition to the instability simulations, the code has been applied to the ZaP Flow Z-Pinch experiment. When resolution is sufficient and simulation conditions match, the results compare favorably to results from MACH2, a 2½D MHD code.

This research demonstrates that MH4D is a useful tool for physics development. Also, MH4D is shown to be useful for qualitative analysis of plasma behavior. High resolution is often needed to capture important details, and in three dimensional simulations is inherently challenging because the degrees of freedom (e.g. the number of tetrahedra) in the computational domain grow with $(1/dx)^3$. The first-order accuracy and the irregular computational grid of MH4D do not maximize computational efficiency. However, the tetrahedral mesh formulation is convenient and flexible. Steadily increasing availability of computational resources might allow useful high-resolution simulations with MH4D. This code development research has only begun to explore the practical utility of MH4D for resistive MHD simulation.

As shown in Section 1.4, resistive MHD does not contain all of the required physics for accurately modeling EC experiments. MH4D is not a practical platform for including the missing physics, in particular the Hall effect and the diamagnetic effect. With these two-fluid effects, the MHD equation system includes high-speed waves that increase in speed with $(1/dx)^2$. A code with first-order spatial accuracy pays a much higher penalty (in the form of small timesteps) for high resolution than a code with higher-order accuracy. Furthermore, the temporal stiffness of the system is such that a fully implicit approach is highly desirable. (A discussion of practical considerations for modeling with two-fluid physics can be found in [36].)

7.2 Future study

Some additional development of MH4D could be pursued. As described in Section 6.4, an important improvement to MH4D would be to develop the semi-implicit method for general use. Furthermore, there is some interest in applying the code to experiments that require full 3D treatment such as the HIT-SI experiment at the University of Washington and the CTIX experiment at the University of California at Davis.

MH4D will likely be used as a platform for additional atomic physics development.

While the "best" formulation for modeling EC experiments, in terms of spatial discretization method and time advance approach, is not obvious, high-order accuracy and implicit time advancement have clear advantages, particularly when two-fluid effects are included. Future study is expected to center on developing a full 3D code based on the SEL code [35]. The code is to be called HI-FI (for **Hi**gh-order **Fi**nite elements). HI-FI features will include a fully implicit time advance, and high-order finite elements on a semi-structured hexahedral domain. Like MH4D, HI-FI will have the flexibility to model complex geometries.

BIBLIOGRAPHY

[1] International Thermonuclear Experimental Reactor – www.iter.org

[2] A. J. Redd et al., *Overview of the Helicity Injected Torus (HIT) program*, J. of Fusion Energy, Vol. 26, Nos. 1-2, June 2007

[3] U. Shumlak, T. W. Hussey, R. E. Peterkin Jr., *Three-dimensional magnetic field enhancement in a liner implosion system*, IEEE Trans. on Plasma Sci., Vol. 23, No. 1, Feb. 1995

[4] U. Shumlak, B. Udrea, *An Approximate Riemann solver for MHD computations on parallel architectures*, AIAA 2001-2591

[5] V. A. Izzo, *Three-dimensional magnetohydrodynamic simulations of the Helicity Injected Torus with Steady Inductive drive*, Phys. Plasmas, Vol. 12, No. 5. May 2005

[6] T. D. Rognlien, *2-D fluid transport simulations of gaseous/radiative divertors*, Contr. Plasma Phys., Vol. 43, No. 2-3, 1994

[7] N. Krall, A. Trivelpiece, Principles of Plasma Physics, McGraw-Hill, 1973

[8] J. P. Freidberg, *Ideal magnetohydrodynamic theory of magnetic fusion systems*, Reviews of Modern Phys., Vol. 54, No. 3, July 1982

[9] R. J. Goldston, P. H. Rutherford, Introduction to Plasma Physics, IOP Publishing Ltd., 1995

[10] R. Lionello, Z. Mikic , D. D. Schnack, *Magnetohydrodynamics of solar coronal plasmas in cylindrical geometry*, J. Comp. Phys., Vol. 140, 1998

[11] R. Lionello, Z. Mikic , J.A. Linker, *Stability of algorithms for waves with large flows*, J. Comp. Phys., Vol. 152, 1999

[12] P. M. Bellan, Spheromaks, Imperial College Press, 2000

[13] M. D. Kruskal, M. Schwarzschild, *Some instabilities of a completely ionized plasma*, Proc. R. Soc. London A, Vol. 223, 1954

[14] V. D. Shafranov, *The Kruskal-Shafranov current limit*, At. Energy, Vol. 5, 1956

[15] G. Bateman, MHD Instabilities, MIT Press, 1978

[16] B. B. Kadomtsev, *Hydromagnetic stability of a plasma*, Reviews of Plasma Physics, Vol. 2, Consultants Bureau, 1966

[17] U. Shumlak, T.K. Fowler, E.C. Morse, *Rotational effects on the m=1 magnetohydrodynamic instability in spheromaks*, Phys. Plasmas, Vol. 1, No. 3, March 1994

[18] ParMETIS Parallel Graph Partitioning software, http://glaros.dtc.umn.edu/gkhome/metis/parmetis/overview

[19] J. Loverich, U. Shumlak, *Nonlinear full two-fluid study of m=0 sausage instabilities in an axisymmetric Z pinch*, Phys. Plasmas, Vol. 13, No. 8, Aug. 2006

[20] A. Hakim, U. Shumlak, *Two-Fluid Physics and Field-Reversed Configurations*, Vol. 14, Phys. Plasmas, 055911, 2007

[21] General Mesh Viewer (GMV) visualization software, http://www-xdiv.lanl.gov/XCM/gmv/GMVHome.html

[22] Tecplot data visualization software, http://www.tecplot.com

[23] R. LeVeque, Finite Volume Methods for Hyperbolic Problems, Cambridge University Press, 2002

[24] D. Rypl, T3D Mesh Generator, http://ksm.fsv.cvut.cz/~dr/t3d.html

[25] W. H. Press, S. A. Teukolsky, W. T. Vetterling, B. P. Flannery, Numerical Recipes, 2nd Ed., Cambridge University Press, 1992

[26] Portable, Extensible Toolkit for Scientific Computation (PETSc) http://www-unix.mcs.anl.gov/petsc/petsc-as/index.html

[27] E. J. Caramana, *Derivation of implicit difference schemes by the method of differential approximation*, J. Comp. Phys., Vol. 96, 1991

[28] D. D. Schnack, D. C. Barnes, Z. Mikic´, D. S. Harned, *Semi-implicit MHD calculations*, J. Comp. Phys., Vol. 70, 1987

[29] D. S. Harned, D. D. Schnack, *Semi-implicit method for long time scale MHD computations in 3D*, J. Comp. Phys., Vol. 65, 1986

[30] S. Vadlamani, *Validation of the semi-implicit algorithm time stepping for MH4D*, J. Fusion Energy, Vol. 26, Nos. 1-2, June 2007

[31] P. Lynch, *The origins of computer weather prediction and climate modeling*, J. Comp. Phys., 2007 (In Press)

[32] R. Golingo et al., *Formation of a Sheared Flow Z-Pinch*, Phys. of Plasmas, Vol. 12, No. 6, June 2005

[33] J. E. Sturtevant, R. E. Peterkin Jr., A. J. Giancola, *Mach2: A reference manual– fifth edition*, Technical Report MRC/ABQ-R-1490, Mission Research Corporation, July 1992

[34] ZaP website, http://www.aa.washington.edu/AERP/ZaP/

[35] A. H. Glasser, X. Z. Tang, *The SEL macroscopic modeling code*, Comp. Phys. Comm., Vol. 164, Issues 1-3, December 2004

[36] D. D. Schnack et. al., *Computational modeling of fully ionized magnetized plasmas using the fluid approximation*, Phys. of Plasmas Vol. 13, 058103, 2006

Appendix A

MH4D Background

A.1 – MH4D Units

MH4D is based on the S.I. units. Ampère's Law (without displacement current) is usually $\nabla\times\mathbf{B}=\mu_0\mathbf{J}$. In MH4D, **B** and **J** are redefined such that the factor of μ_0:is distributed. $\mathbf{B}_{\mathrm{M}}$ = $\mathbf{B}\big/\sqrt{\mu_0}$ and $\mathbf{J}_{\mathrm{M}}$ $=\mathbf{J}\sqrt{\mu_0}$. Ampère's Law becomes $\nabla\times\mathbf{B}_M=\mathbf{J}_M$ where the "M" subscript is for "MH4D units". Given that **B** is the curl of **A**, clearly $\mathbf{A}_{\mathrm{M}}=\mathbf{A}\big/\sqrt{\mu_0}$.

The induction equation is $\frac{\partial\mathbf{A}}{\partial t}=\mathbf{v}\times\mathbf{B}-\eta\mathbf{J}$ or in MH4D units, $\frac{\partial\mathbf{A}_M}{\partial t}=\mathbf{v}\times\mathbf{B}_M-\eta_M\mathbf{J}_M$. From this equation, it is clear that $\eta_{\mathrm{M}}=\eta/\mu_0$. The other variables (velocity, density, pressure and time) retain their original S.I. units. In summary:

Variable	Conversion
t	n/a
p	n/a
ρ	n/a
V	n/a
A	$\mathbf{A}_{\mathrm{MH4D}}=\mathbf{A}\big/\sqrt{\mu_0}$.
B	$\mathbf{B}_{\mathrm{MH4D}}=\mathbf{B}\big/\sqrt{\mu_0}$.
J	$\mathbf{J}_{\mathrm{MH4D}}=\mathbf{J}\sqrt{\mu_0}$.
η	$\eta_{\mathrm{MH4D}}=\eta/\mu_0$.

A.2 – MH4D Grid Information Data Structure

A spreadsheet showing the MH4D grid information data structure after parallelization is shown in Figure A1 (in the code, the "geometry" subroutine contains comments describing the global reference arrays). The variables shown in Figure A1 are declared in the header of the MH4D module tetrahedralgrid.f. As shown, derived type objects are created for vertices, tetrahedra, sides, and edges. Within those objects is information like location, neighbors, surface area vectors, boundary flags, etc.

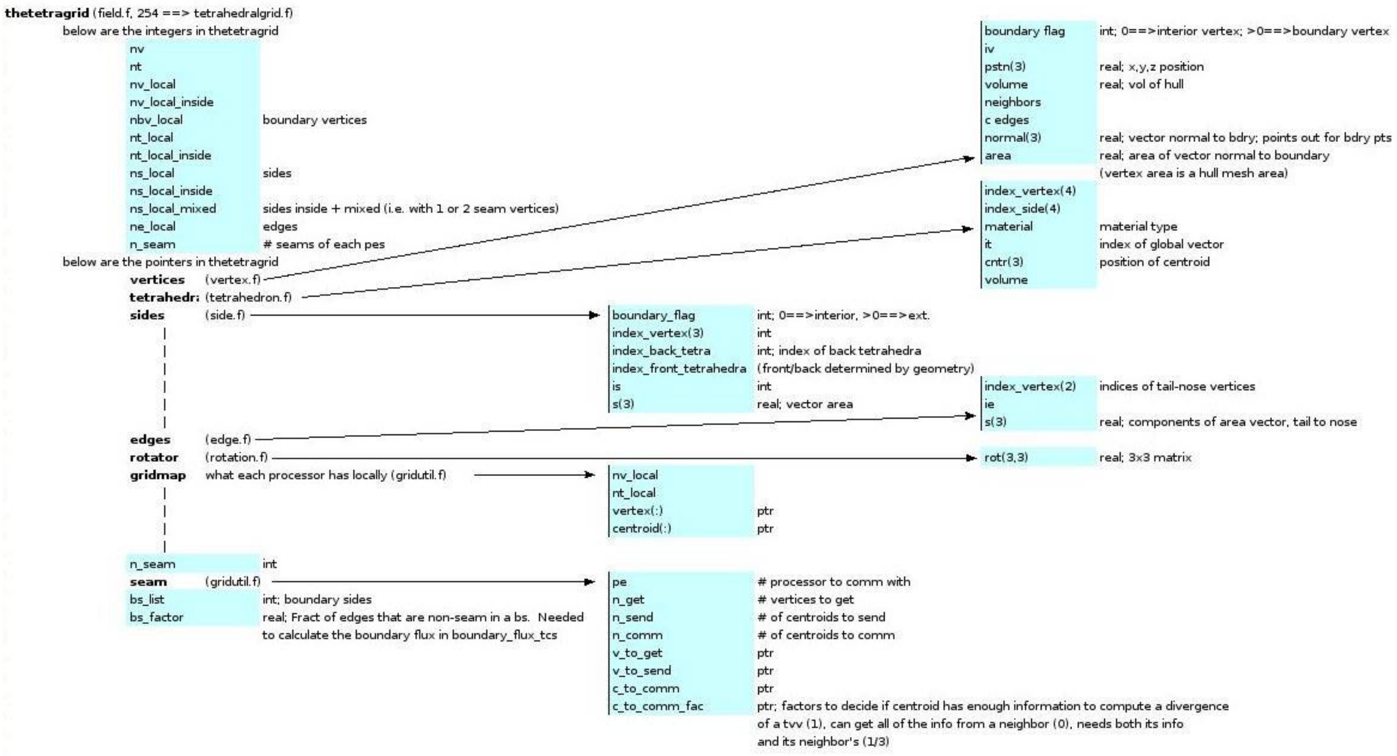
thetetragrid (field.f, 254 ==> tetrahedralgrid.f)
below are the integers in thetetragrid
nv
nt
nv_local
nv_local_inside
nbv_local boundary vertices
nt_local
nt_local_inside
ns_local sides
ns_local_inside
ns_local_mixed sides inside + mixed (i.e. with 1 or 2 seam vertices)
ne_local edges
n_seam # seams of each pes
below are the pointers in thetetragrid
vertices (vertex.f)
tetrahedr: (tetrahedron.f)
sides (side.f)
edges (edge.f)
rotator (rotation.f)
gridmap what each processor has locally (gridutil.f)
n_seam int
seam (gridutil.f)
bs_list int; boundary sides
bs_factor real; Fract of edges that are non-seam in a bs. Needed to calculate the boundary flux in boundary_flux_tcs
boundary flag int; 0==>interior vertex; >0==>boundary vertex
iv
pstn(3) real; x,y,z position
volume real; vol of hull
neighbors
c edges
normal(3) real; vector normal to bdry; points out for bdry pts
area real; area of vector normal to boundary
(vertex area is a hull mesh area)
index_vertex(4)
index_side(4)
material material type
it index of global vector
cntr(3) position of centroid
volume
boundary_flag int; 0==>interior, >0==>ext.
index_vertex(3) int
index_back_tetra int; index of back tetrahedra
index_front_tetrahedra (front/back determined by geometry)
is int
s(3) real; vector area
index_vertex(2) indices of tail-nose vertices
ie
s(3) real; components of area vector, tail to nose
rot(3,3) real; 3x3 matrix
nv_local
nt_local
vertex(:) ptr
centroid(:) ptr
pe # processor to comm with
n_get # vertices to get
n_send # of centroids to send
n_comm # of centroids to comm
v_to_get ptr
v_to_send ptr
c_to_comm ptr
c_to_comm_fac ptr; factors to decide if centroid has enough information to compute a divergence of a tvv (1), can get all of the info from a neighbor (0), needs both its info and its neighbor's (1/3)

Figure A1: MH4D Grid Information Data Structure

A.3 – MH4D Geometry Information and Proof that $\nabla \bullet \mathbf{B} = 0$ Inside the Domain

This appendix section provides a proof that the divergence of magnetic field is zero and briefly discusses some important computational characteristics of MH4D. The appropriate geometric preliminaries are provided. This appendix section is based on unpublished work by D. Schnack and R. Lionello.

In the MHD model, the vector potential, **A**, the magnetic field, **B**, and the current density, **j**, are related by the curl operator,

$$\mathbf{B} = \nabla \times \mathbf{A}\,, \tag{A1}$$

$$\mathbf{j} = \nabla \times \mathbf{B}\,, \tag{A2}$$

and so

$$\mathbf{j} = \nabla \times \nabla \times \mathbf{A}\,. \tag{A3}$$

As required by Eqns. (A1) and (A2), $\nabla \bullet \mathbf{B} = 0$ and $\nabla \bullet \mathbf{j} = 0$. The second order differential operator in Eqn. (A3) is self-adjoint. Ideally, a computational MHD code should preserve these solenoidal and self-adjoint properties.

Some geometric preliminaries are now given to provide a basis for the discussion that follows. A tetrahedral cell of the primary mesh is shown in Figure A2.

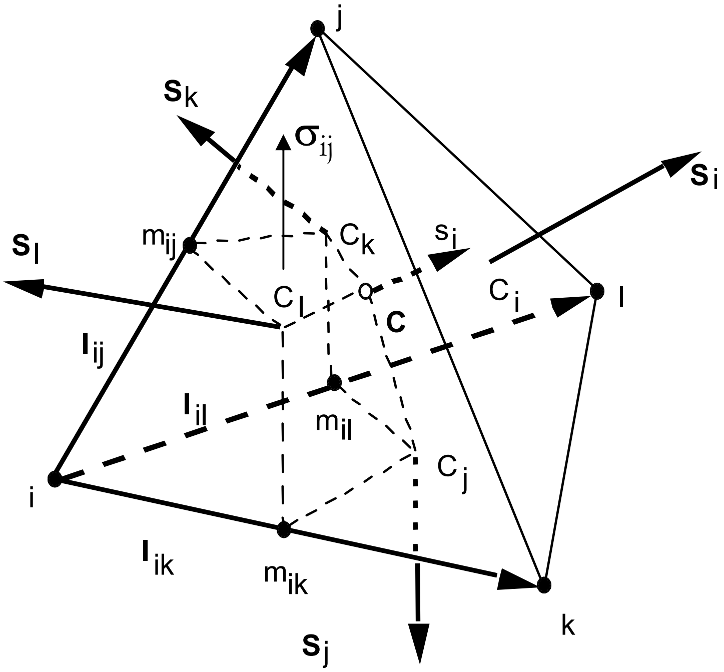

Figure A2: Tetrahedral grid cell

The centroid of the cell is labeled C. The vertices are labeled *i*, *j*, *k*, and *l*. Vertices *j*, *k*, and *l* are ordered clockwise as seen from vertex *i*. The triangular sides are labeled by the index of their opposing vertex. The area vectors for the sides, $\mathbf{S}_i = S_i \hat{\mathbf{n}}_i$, are pointed out of the cell.

The cross product of two edge vectors of a side give the area, e.g., $\mathbf{S}_i = \frac{1}{2} \mathbf{l}_{ik} \times \mathbf{l}_{ij}$. The area vectors satisfy the relationship

$$\sum_{i=1}^{4} \mathbf{S}_i = 0 . \quad \text{(A4)}$$

A second mesh is intertwined with the mesh of tetrahedral cells. This "dual mesh" is shown in dashed lines inside the tetrahedral cell in Figure A2. It can be shown that the points C, C_l, C_k, and m_{ij} are coplanar. The quadrilateral defined by those four points, indicated by $\boldsymbol{\sigma}_{ij}$, is one of three areas that form the surface of the dual mesh volume inside of the cell that encloses vertex *i*. It can be shown that the dual mesh surface area inside the cell τ enclosing vertex *i* is $\mathbf{s}_i^\tau = \frac{1}{3}\mathbf{S}_i^\tau$. The volume of the dual mesh enclosing vertex *i* within cell τ is $v_i^\tau = \frac{1}{4}V_\tau$. The total dual mesh volume enclosing vertex *i* is then $v_i = \sum_\tau v_i^\tau$ where the sum is over tetrahedra that share vertex *i*.

The vector potential **A** is defined at vertices. Using a finite volume representation, magnetic field **B** is defined at cell centers in terms of **A**, and current density **j** is defined at vertices in terms of **A**.

A generalization of Stokes' theorem relates the volume integral of a curl to the integral of the vector over the control surface,

$$\int \nabla \times \mathbf{A} dV = \oint d\mathbf{S} \times \mathbf{A} . \tag{A5}$$

Applying Eqn. (A5) to tetrahedral cell τ,

$$\mathbf{B}_\tau V_\tau = \sum_{i=1}^{4} \mathbf{S}_i \times \overline{\mathbf{A}}_i , \tag{A6}$$

where the sum is over the four triangular faces, and, for example, $\overline{\mathbf{A}}_i$ is

$$\overline{\mathbf{A}}_i = \frac{1}{3}\left(\mathbf{A}_j + \mathbf{A}_k + \mathbf{A}_l\right) \tag{A7}$$

Then, using Eqn. (A4), Eqn. (A7) can be rewritten

$$\mathbf{B}_\tau = -\frac{1}{3V_\tau}\sum_{i=1}^{4}\mathbf{S}_i \times \mathbf{A}_i\,, \tag{A8}$$

where the sum is now over the four vertices of the tetrahedron. Eqn. (A8) is the primary definition of **B** in terms of **A**.

The divergence of **B** is computed using Gauss' theorem,

$$\int \nabla \bullet \mathbf{B}\,dV = \oint \mathbf{B} \bullet d\mathbf{S}\,, \tag{A9}$$

which is applied to the dual mesh volume element enclosing each vertex,

$$\left(\nabla \bullet \mathbf{B}\right)_i v_i = \sum_\tau \mathbf{B}_\tau \bullet \mathbf{s}_i^\tau\,, \tag{A10}$$

where v_i is the dual mesh volume around vertex *i*, the sum is over the tetrahedra, τ, surrounding vertex *i*, and $\mathbf{s}_i^\tau$ is the dual mesh area in tetrahedron τ associated with vertex *i*. This can be rewritten in terms of **A**,

$$\begin{aligned}\left(\nabla \bullet \mathbf{B}\right)_i v_i &= \sum_\tau \frac{1}{3V_\tau}\sum_{\gamma=i,j,k,l}\bar{\mathbf{A}}_\gamma^\tau \bullet \left(\mathbf{S}_i^\tau \times \mathbf{S}_\gamma^\tau\right) \\ &= \sum_\tau \frac{1}{3V_\tau}\begin{bmatrix}\bar{\mathbf{A}}_j^\tau \bullet \left(\mathbf{S}_i^\tau \times \mathbf{S}_j^\tau\right) + \bar{\mathbf{A}}_k^\tau \bullet \left(\mathbf{S}_i^\tau \times \mathbf{S}_k^\tau\right) \\ +\bar{\mathbf{A}}_l^\tau \bullet \left(\mathbf{S}_i^\tau \times \mathbf{S}_l^\tau\right)\end{bmatrix}.\end{aligned} \tag{A11}$$

Consider two adjacent tetrahedra sharing vertex *i*, τ_1 and τ_2, as shown in Figure A3. Their common interface is shaded in the figure.

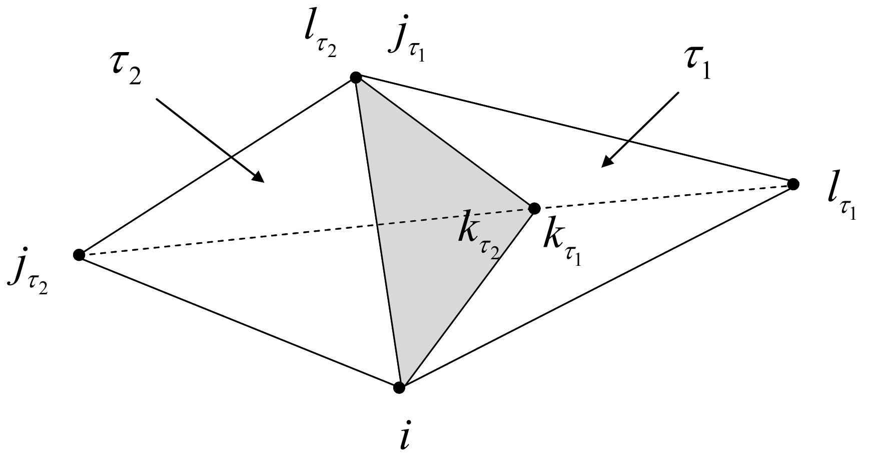

Figure A3: Two tetrahedra that share vertex *i*. Their common interface is shaded.

The terms from the common interface triangles are

$$3(\nabla \bullet \mathbf{B})_i v_i = \ldots + \frac{1}{V_{\tau_1}} \overline{\mathbf{A}}_{l_1}^{\tau_1} \bullet \left(\mathbf{S}_i^{\tau_1} \times \mathbf{S}_{l_1}^{\tau_1}\right) + \frac{1}{V_{\tau_2}} \overline{\mathbf{A}}_{j_2}^{\tau_2} \bullet \left(\mathbf{S}_i^{\tau_2} \times \mathbf{S}_{j_2}^{\tau_2}\right) + \ldots, \qquad \text{(A12)}$$

It can be shown that

$$\mathbf{S}_i^{\tau_1} \times \mathbf{S}_{l_1}^{\tau_1} = \frac{3}{2} V_{\tau_1} \mathbf{l}_{k_1 j_1}, \qquad \text{(A13)}$$

and

$$\mathbf{S}_i^{\tau_2} \times \mathbf{S}_{j_2}^{\tau_2} = -\frac{3}{2} V_{\tau_2} \mathbf{l}_{k_2 l_2}. \qquad \text{(A14)}$$

Now Eqn. (A12) can be written

$$2(\nabla \bullet \mathbf{B})_i v_i = \ldots + \overline{\mathbf{A}}_{l_1}^{\tau_1} \bullet \mathbf{l}_{k_1 j_1} + \overline{\mathbf{A}}_{j_2}^{\tau_2} \bullet \mathbf{l}_{k_2 l_2} + \ldots. \qquad \text{(A15)}$$

By construction, $\overline{\mathbf{A}}_{l_1}^{\tau_1} = \overline{\mathbf{A}}_{j_2}^{\tau_2}$ and $\mathbf{l}_{k_1 j_1} = \mathbf{l}_{k_2 l_2}$, so the contributions from the common faces cancel and $\left(\nabla \bullet \mathbf{B}\right)_i = 0$. That is, the divergence of **B** vanishes at interior vertices. In simulations, it has been found that $\nabla \bullet \mathbf{B} = 0$ is not enforced at boundary vertices in the current implementation.

Using the same Stokes' theorem approach, but now applied to the dual mesh volume around a vertex, the current density **j** is defined

$$\mathbf{j}_i v_i = \frac{1}{3} \sum_{\tau} \mathbf{S}_{\tau} \times \mathbf{B}_{\tau} . \tag{A16}$$

By inserting the expression for **B** given in Eqn. (A8), it can be shown that Eqn. (A16) becomes

$$\mathbf{j}_i v_i = -\frac{1}{9} \sum_{\tau} \frac{1}{V_{\tau}} \sum_{j=1}^{4} \left[\mathbf{S}_j^{\tau} \mathbf{S}_i^{\tau} - \left(\mathbf{S}_i^{\tau} \bullet \mathbf{S}_j^{\tau} \right) \mathbf{I} \right] \bullet \mathbf{A}_j^{\tau} \tag{A17}$$

This can be written as

$$\mathbf{j}_{\nu} v_{\nu} = \sum_{\tau(\nu)} \sum_{\nu(\tau)} \mathcal{M}^{\tau} \left(\nu, \nu' \right) \bullet \mathbf{A}_j^{\tau} , \tag{A18}$$

where ν indicates a vertex, $\tau(\nu)$ indicates a tetrahedron that shares vertex ν, and $\nu(\tau)$ is a vertex of tetrahedron $\tau(\nu)$. This operator, $\mathcal{M}^{\tau}$ is symmetric and self-adjoint.

The more complicated geometry involved in Eqn. (A17) has prevented theoretical analysis of $\nabla \bullet \mathbf{j}$ (a quantity stored at cell centers). However simulations show that $\nabla \bullet \mathbf{j} = 0$ is not enforced in the current implementation.

In summary, the MH4D formulation ensures $\nabla \bullet \mathbf{B} = 0$ for interior vertices. Furthermore, the double curl operator is self-adjoint. However, $\nabla \bullet \mathbf{B} = 0$ is not enforced at boundaries, and $\nabla \bullet \mathbf{j} = 0$ is not enforced.

Appendix B

T3D Grid Generation

The website for T3D (http://mech.fsv.cvut.cz/~dr/t3d.html) has a user guide, and several sample input files.

Below is a sample t3d input file.

```
# A simple 2x2x2 box

vertex 11 xyz 0. 0. 0.
vertex 12 xyz 0. 0. 2.
vertex 13 xyz 0. 2. 2.
vertex 14 xyz 0. 2. 0.
vertex 15 xyz 2. 0. 0.
vertex 16 xyz 2. 0. 2.
vertex 17 xyz 2. 2. 2.
vertex 18 xyz 2. 2. 0.

curve 12 order 2 vertex 11 12
curve 23 order 2 vertex 13 12
curve 34 order 2 vertex 14 13
curve 41 order 2 vertex 14 11
curve 56 order 2 vertex 15 16
curve 67 order 2 vertex 17 16
curve 78 order 2 vertex 18 17
curve 85 order 2 vertex 18 15
curve 15 order 2 vertex 11 15
curve 26 order 2 vertex 12 16
curve 48 order 2 vertex 14 18
curve 37 order 2 vertex 13 17

surface 15 curve 12 26 56 15 output yes
surface 16 curve 34 37 78 48 output yes

surface 11 curve 12 23 34 41 output yes
surface 13 curve 56 67 78 85 output yes

surface 12 curve 26 23 37 67 output yes
surface 14 curve 15 41 48 85 output yes

region 31 boundary surface -11 12 13 -14 15 -16 size def
```

With this input file, the command to discretize this 2x2x2 box into tetrahedra with maximum edge length 0.1 and write the output file box.t3d is

```
> t3d -i box.in -o box.t3d -d 0.1
```

A useful T3D feature is its ability to control grid packing by using “background mesh” files. This feature is critical for generating efficient meshes. For a screw pinch simulation, for instance, it may be important to have a fine mesh near the axis of a cylindrical domain, and a smooth transition to coarse mesh near the cylinder wall. The procedure for using background mesh files is detailed in the online manual.